Classical Flutter Analysis of X-57 Aircraft Mod II, III, and IV Configurations

Keerti K. Bhamidipati[1] and Chan-gi Pak[2],
NASA Armstrong Flight Research Center, Edwards, California, 93523, U.S.A.

Roger Truax[3],
Retired, NASA Armstrong Flight Research Center, Edwards, California, 93523, U.S.A.

James P. Winkel[4], Sev Rosario[5], Stephen E. Cutright[6],
Steven J. Massey[7], and Carol D. Wieseman[8]
NASA Langley Research Center, Hampton, Virginia, 23666, U.S.A.

To support airworthiness assessment of the X-57 electric propulsion demonstrator aircraft, the National Aeronautics and Space Administration (NASA) completed classical flutter analysis of the Mod II, Mod III, and Mod IV aircraft configurations. Aeroelastic analysis was primarily performed using the ZAERO analysis code developed by Zona Technology. Supplemental computational fluid dynamics (CFD) flutter analysis for the Mod III and Mod IV configurations was performed using NASA's FUN3D software to verify the aeroelastic behavior at deployed flaps conditions. The NASTRAN finite element models (FEMs) used for aeroelastic analysis were developed by NASA. The final Mod II FEM utilized shell elements for the wing and fuselage, and beam elements for the tail and wing control surfaces. For Mod III and Mod IV aircraft models, shell element wing FEMs developed throughout the Mod III/IV wing design cycle were utilized. The fuselage and empennage FEM components were shared between the Mod II, III, and IV aircraft models. ZAERO analyses predicted flutter boundaries were >60% beyond the X-57 flight-test envelope never exceed airspeed (V_{NE}) for all configurations. Aeroelastic Reynolds-averaged Navier–Stokes (RANS) CFD simulations using FUN3D of the Mod III/IV configurations predicted flap mode instability did not occur until at least speeds of 60% higher than the Mod III/IV maximum flap deployment airspeed (V_{FE}).

I. Nomenclature

V_D = vehicle design dive airspeed
V_{FE} = maximum flaps extended airspeed
V_{NE} = vehicle never exceed airspeed
V_S = power off vehicle stall airspeed in cruise configuration
V-g = damping versus velocity
ζ = damping

[1] Aerospace Engineer, Aerostructures Branch (AFRC-560), Senior AIAA Member.
[2] Analytical Structural Dynamics SME/Aerospace Engineer, Aerostructures Branch (AFRC-560).
[3] Retired, Aerostructures Branch (AFRC-560).
[4] Structural Dynamics Engineer, Structural and Thermal Systems Branch (LARC-D206).
[5] Aerospace Engineer, Structural and Thermal Systems Branch (LARC-D206).
[6] Aerospace Engineer, Structural and Thermal Systems Branch (LARC-D206).
[7] Research Aerospace Engineer, Aeroelasticity Branch (LARC-D308), Senior AIAA Member.
[8] Senior Aerospace Engineer, Aeroelasticity Branch (LARC-D308), AIAA Associate Fellow.

II. Background

The X-57 "Maxwell" aircraft was an electric propulsion demonstrator aircraft developed by the National Aeronautics and Space Administration (NASA) to inform airworthiness standards for electrified aircraft. The airframe was a modified general aviation Tecnam P2006T airplane built by Costruzioni Aeronautiche Tecnam (Capua, Italy) [1, 2]. Illustrations of the X-57 Mod II, III, and IV aircraft configurations are shown in Fig. 1. Flutter analyses of the Mod II, Mod III, and Mod IV X-57 aircraft configurations were performed to evaluate the airworthiness of the X-57 sufficient to satisfy flight-test research objectives. Research flight tests at the NASA Armstrong Flight Research Center (AFRC) utilize a risk-based approach to self-certify and have no requirement to clear aircraft flying in a controlled airspace to vehicle design dive airspeed (V_D). Flight-test pilots are provided an aircraft never exceed airspeed (V_{NE}) requirement which must be maintained throughout the test program.

Aeroelastic classical flutter analysis for the X-57 aircraft was mainly performed using the ZAERO analysis code developed by ZONA Technology, Inc. (Scottsdale, Arizona) [3]. Supplementary flutter analysis on the Mod III and Mod IV configurations to verify whether flap-lateral motion contributed to the aircraft flutter mechanism was performed using the NASA FUN3D computational fluid dynamics (CFD) software. The finite element models (FEMs) utilized for aeroelastic analysis were developed using MSC NASTRAN (MSC Software Corporation, Newport Beach, California). The aircraft structural modes obtained by way of normal modes analysis (SOL103) from MSC NASTRAN were read into ZAERO and FUN3D. Coupling these structural modes with respective ZAERO or FUN3D aerodynamic models yielded classical flutter predictions for the Mod II, III, and IV aircraft configurations.

The X-57 Mod II aircraft, like the Tecnam P2006T airplane on which it is based, utilizes an all-aluminum airframe construction. To build X-57 Mod II, a P2006T without its high wing-mounted gasoline-powered motors, fuel tanks, and internal combustion engine (ICE) accessories was fit with two electrical motors of a similar power class to the ICE motors. Bespoke motor trusses were fabricated to attach electric motors to the same wing firewall locations used by the P2006T gasoline-powered motors. The electric powertrain hardware (e.g., motor controllers, avionics, wiring) were housed primarily inside the aircraft wing. Structurally, the resulting Mod II aircraft wing was ~100 lb lighter than a stock P2006T wing. Additionally, the weight of the wing would remain constant throughout the Mod II flight because the wing contained no gasoline for fuel. The Mod II aircraft fuselage was modified to hold sixteen traction battery modules for powering the electric motors. The ~800 lb of batteries comprised nearly one-third of the total weight of the Mod II aircraft and increased the total weight by ~150 lb compared to the heaviest P2006T. No modifications were made to the P2006T empennage or control system.

The X-57 Mod III/IV aircraft planned to utilize a new-construction high-aspect-ratio carbon-fiber composite wing to replace the Mod II aluminum wing. The Mod III/IV wing would have attached to the aluminum Mod II fuselage using the same four connection points utilized by the Mod II and P2006T wings. In Mod III, the same electric motors used during Mod II were planned to be relocated to the wingtips, significantly altering the moment of inertia and modal characteristics of the wing. For Mod IV an additional 12 high-lift (HL) electric motors, each weighing ~16 lb, were planned to be distributed along wingspan, attached to the carbon-fiber wing. The projected gross weight of the Mod IV aircraft increased to 3,200 lb, compared to the maximum certified weight of the 2,712-lb Tecnam P2006T airplane.

III. Finite Element Models

The NASTRAN FEMs used for aeroelastic analysis were developed by NASA. The Mod II aircraft aeroelastic FEM was primarily built after the Mod II aircraft ground vibration test (GVT) was completed. For Mod III and Mod IV aircraft models, shell element wing FEMs that were developed by NASA throughout the Mod III/IV wing design cycle were utilized. The fuselage and empennage FEM components were shared between the Mod II, III, and IV aircraft models.

A. The Finite Element Model of the Mod II Aircraft

The entire Mod II aircraft structure was initially modeled using only beam-type elements in the FEM [4]. However, attempting to correlate this beam FEM with the Mod II aircraft GVT results [5] revealed the FEM was unable to accurately capture the structural dynamics of the wing/fuselage and stabilator/aft-fuselage structural interfaces. Early efforts to improve FEM fidelity at these interfaces are presented in Fig. 2. The design of the P2006T inner wing section provides greater passenger space and accommodates a top-side emergency escape hatch. As a result, the front spar, which makes up part of the inner wing section torsion box, is located at ~35% chord. The wing is connected to the fuselage by four forks located at the corners of the inner wing section. This design, along with the inability of beam-beam connections to capture the Mod II empennage porpoising mode linked to the wing fore-aft mode, prevented

modeling the wing using only spar beam elements. The empennage porpoising mode was identified as significant for the Mod II aircraft from early flutter predictions. An intermediate wing FEM attempted using shell elements to model the fuselage-connected inner section, and beam elements to model the outer wing sections, as depicted in Fig. 2(a); however, given the verification and validation work necessary to ensure structural dynamics were properly modeled across the shell-to-beam elements transition between wing inner and outer sections, the decision was made to model the entire wingspan using shell elements. Another image showing the intermediate FEM of the stabilator/aft-fuselage attachment is presented in Fig. 2(b). The Tecnam P2006T airplane incorporates a stabilator (an all-moving horizontal tail) with zero-pitching-moment design, which provides excellent flying qualities for pilot control. Modeling the structural dynamics of this stabilator, however, was more complex than modeling those of a traditional fixed horizontal tail having a hinged elevator. The stabilator-fuselage attachment when modeled only utilizing beam elements and springs did not properly represent the structural dynamics of the stabilator with its large mass balance and its connection to the aft fuselage. Once again, shell elements were necessary to model the brackets used to attach the stabilator to the aft fuselage with sufficient fidelity. While early FEM efforts attempted attachment of a shell FEM stabilator bracket to the beam fuselage elements (Fig. 2(b)), again the decision was made to model the entire fuselage skin and all fuselage bulkheads using shell elements.

The final Mod II FEM utilized shell and beam elements for the fuselage and wing components, and only beam elements for the empennage, ailerons, flaps, wingtips, noseboom, and motor components. This approach resulted in a FEM which captured participant modes in the predicted Mod II flutter mechanisms. An image of the final Mod II aircraft FEM is presented in Fig. 3(a). Images of significant Mod II aircraft mode shapes are presented in Figs. 3(b)-(e). The tradeoff of using a shell-element model for flutter simulations is that the aeroelastic solver must be able to handle local panel deformation modes that may be present. Examples of local panel modes observed at higher frequencies are shown in Figs. 3(d)-(e). The final Mod II FEM did not meet the requirements specified in NASA-STD-5002 [6] for significant modes: that (1) FEM natural frequencies must be within 5% of GVT natural frequencies; and (2) FEM shapes have cross-orthogonality values > 0.9, with off-diagonal terms < 0.1. The frequency and cross-orthogonality values for the final Mod II FEM are presented in Fig. 4. The results showed that additional improvements to the FEM model were possible if further structural test data (e.g., mass properties, GVT) could be gathered and incorporated into the FEM. One such improvement might be the addition of accelerometer instrumentation to the stabilator mass balance during aircraft GVT. The mass balance was difficult to access, but due to its relative mass and moment arm, had a significant effect on the structural dynamics of the stabilator. The Mod II aircraft FEM is considered reasonably well correlated up to ~20 Hz. A summary of the Mod II aircraft modes, frequencies, and GVT-measured damping values [5] are presented in Table 1. Additionally, significant modes of the Mod II aircraft as determined by ZAERO flutter analysis are highlighted in Table 1. These highlighted modes are the ones subject to NASA-STD-5002 frequency and cross-orthogonality requirements for a validated FEM. Flutter analysis completed using the final Mod II FEM yielded flutter predictions sufficient to satisfy the flight-test objectives of the X-57 project.

B. The Finite Element Model of the Mod III/IV Aircraft

The Mod III full aircraft FEM consisted of the correlated fuselage and empennage parts from the Mod II FEM, combined with a Mod III wing model correlated using static load test and GVT data. The Mod III wing/aircraft FEM only included two large wingtip cruise motor electric propulsion units (no HL motors). Wing, flap, aileron, and wingtip nacelle structures were modeled using shell elements, and wingtip motors were represented by concentrated masses connected to their nacelles using rigid body elements (RBEs). Images of the Mod III aircraft FEM and significant mode shapes are presented in Fig. 5. The Mod IV wing/aircraft FEM added HL nacelle and motor components to the Mod III wing FEM. Images of the Mod IV aircraft FEM and significant mode shapes are presented in Fig. 6. Analogous to the wingtip cruise motors, the additional 12 HL nacelle structures were modeled using shell elements, and the 12 HL motors are represented by concentrated masses connected to the HL nacelles using RBEs.

Since the Mod III wing GVT was conducted prior to the fabrication of wingtip cruise motor nacelles, correlation efforts were limited to the wing and flap structure. Cruise motor mass substitutes were attached at the Mod III wingtip to simulate the weight of the cruise motors. The flap position setting - stowed, slightly deployed, or (fully) deployed - had a significant effect on the Mod III wing control surface modes, and flap contact effects had to be modeled for successful correlation. Specifically, flap/cove contact was modeled using very flexible CBUSH elements (< 5 lb/in stiffness), and right and left flap contact stiffness values were independently specified. Unfortunately, correlation of the Mod IV wing FEM was not feasible, since fabrication of the HL motor nacelles and HL mounting brackets was not completed. Furthermore, since fabrication of flap hinge lateral support brackets which had to be connected to the HL mounting brackets, was not complete, the Mod III wing flaps exhibited non-linear/loose mechanism modes during the wing GVT.

The Mod III wing FEM correlation started with a CAD-versus-FEM review and included updating the wing FEM to match the as-built wing structure. Afterward, numerical correlation focused primarily on the joints, where most FEM inaccuracy is traditionally found. Non-realistic changes such as elastic modulus or density variation were not allowed. Optimization of FEM stiffness values was performed using Attune™ software (ATA Engineering, Inc., San Diego, California) [7]. During optimization, utilizing a combination of strain energy distributions and past model correlation experience, well-defined limits for each parameter being modified were chosen to ensure all FEM modifications were well grounded and justifiable. The frequency and cross-orthogonality values for the Mod III wing FEM with flaps in stowed and deployed positions are presented in Fig. 7 and Fig. 8, respectively. The cross-orthogonality plots show fundamental wing modes and primary flap bending modes up to ~40 Hz were well correlated, but also highlight some limitations that were encountered. The Mod III wing GVT was performed on a fixture designed for the wing loads proof test. This test fixture had flexible modes starting at ~40 Hz, which affected the GVT-measured mode shapes. A FEM of the test stand was included during the FEM-GVT correlation, but even more accelerometer instrumentation measuring test stand modes was required (and not available) to improve wing mode correlation ≥ 40 Hz. Another challenge noted was a FEM-versus-GVT difference where no significant response corresponding to FEM modes 7 and 8 (flap modes) was measured during GVT with flaps stowed (Fig. 7). These flap modes were restrained by contact with the wing flap-cove surface when flaps were in the stowed position. Further analysis of GVT data revealed that control surface modes > 30 Hz changed frequency and damping significantly at different shaker input levels (indicating non-linearity in flap modes), and that GVT-measured damping values of control surface modes were 4 to 8 times larger than those of the wing modes. The high damping values measured for control surface modes help alleviate concerns that the Mod III wing FEM is not well correlated at higher frequencies. Since GVT-measured damping is the lower in magnitude (more conservative) than damping experienced during flight loading, flutter analysis is expected to overpredict Mod III/IV wing control surface mode response compared to the in-flight structural dynamics.

IV. ZAERO Flutter Predictions

NASA ZAERO aeroelastic models predicted the primary Mod II flutter mechanism to be a stabilator rotation mode coupled with an empennage porpoising mode, followed by a higher-speed secondary mechanism driven by stabilator rotation, fuselage bending, and stabilator bending. The Mod III flutter mechanisms were predicted to be a primary mechanism driven by wing bending-torsion behavior, followed by a higher-speed secondary mechanism driven by stabilator rotation, fuselage bending, and stabilator bending. In the Mod IV configuration, addition of distributed high-lift motor masses along the wingspan shifted the wing torsion mode frequency and resulted in no bending-torsion flutter predicted for the Mod IV wing aircraft. The Mod IV primary flutter mechanism was predicted to be coupling between stabilator rotation, fuselage bending, and stabilator bending modes. These results are discussed in greater detail in the following subsections.

A. Mod II ZAERO Flutter Predictions

The unsteady aerodynamic model employed for the Mod II ZAERO flutter analysis is depicted in Fig. 9(a). Body-type aerodynamic panel elements were used to model the fuselage, noseboom, and motor nacelles. Flat-plate type panel elements were used to model the wing, tail, and control surfaces. The model consisted of 3335 aerodynamic panel elements and represented the entire aircraft. An initial ZAERO unsteady aerodynamic model consisting of only wing and tail components modeled using flat-plate type panel elements, and is shown in Fig. 9(b). The initial wing and tail aerodynamic model was sufficient for aeroelastic analysis, but yielded more conservative flutter predictions (flutter predicted to occur at lower airspeeds) than the final unsteady aerodynamic model shown in Fig. 9(a). The participant modes and flutter mechanism predicted by ZAERO did not change between the two aerodynamic models.

ZAERO matched point flutter analysis across Mach numbers 0.2 to 0.6 using the G-method flutter solution technique [8] provided predicted aeroelastic damping and frequency as functions of velocity. For these analyses 17 reduced frequencies ranging from zero to one were used to compute aerodynamic influence coefficient (AIC) matrices. The AICs provide structurally independent aerodynamic forces. Figure 10 displays the reduced frequencies at Mach 0.3, and illustrates that the first and second flutter modes for the Mod II aircraft fall within the range of reduced frequencies used for AIC matrix calculations (i.e., no extrapolation of AIC matrix occurred around the predicted flutter modes). For Mod II flutter analysis, the first 60 natural FEM modes were included in the ZAERO input. When using ZAERO, the recommended practice is to include FEM modes up to 3 times the frequency at which flutter is predicted, to aid solution convergence and residual management within the solver. The analyst should treat with caution any flutter predicted to be driven by modes outside FEM-validated frequencies. The modal participation factors (MPFs) at the Mach 0.3 flutter crossing for the Mod II configuration are presented in Table 2. Modal

participation factors indicate how strongly individual FEM modes contribute to the predicted flutter mechanism. The highlighted modes on Table 2 show the two modes which contribute most to the first and second flutter mechanisms are within the Mod II FEM-validated frequency range.

Predicted damping versus velocity (V-g) curves for the Mod II aircraft from matched point flutter analyses at Mach numbers of 0.2 to 0.6 are presented in Fig. 11 and Fig. 12. Figures 11(a)-(d) show the V-g curves from simulations that included no structural damping in the ZAERO input and employ 0% and 2% damping crossings to determine flutter speeds. Meanwhile, Figs. 12(a)-(d) show the V-g curves from ZAERO analysis which used GVT-measured damping value (shown on Table 1). In Fig. 12 the 0% damping crossing establishes flutter boundaries. A summary of predicted flutter speeds and frequencies are presented in Table 3. Two unstable mechanisms are shown on the V-g plots in Fig. 11 and Fig. 12: (1) a hump-mode instability predicted at 185-284 knots equivalent airspeed (KEAS); and (2) a catastrophic instability predicted at 345-409 KEAS. For ZAERO analysis without structural damping specified for individual FEM modes, the hump-mode instability only exceeds the 2% damping line for the Mach 0.5 flight condition (as shown in Fig. 11(d)), resulting in a first flutter crossing with a margin ~50% against V_{NE}. The catastrophic instability second flutter crossing exceeds the 2% damping line at Mach 0.4, and 0.5 conditions (as shown in Figs. 11(c-d)). For ZAERO analysis using GVT measured damping (shown in Fig. 12), the hump-mode was not predicted to cross over to the unstable region, but the catastrophic instability flutter crossing is predicted at Mach 0.4, 0.5, and 0.6 conditions (as shown in Figs. 12(b-d).

The predicted Mod II flutter crossings plotted on an X-57 project flight envelope are shown in Fig. 13. The first flutter mode is represented by blue rectangles, while the second flutter mode is represented by green triangles. Since the first flutter mode 2% damping instability threshold is only exceeded at the Mach 0.5 condition, the maximum damping blue rectangle points for the Mach 0.3 and 0.4 conditions are filled in red and yellow colors, respectively, and are not connected by any line to indicate a boundary. For the second flutter mode, the difference between the 2% assumed damping and GVT-measured damping results are difficult to distinguish on the flight envelope plot. Most of the green 2% damping boundary line for the second flutter mode is hidden under the green solid measured-damping boundary line - only a minute variance in the Mach 0.5 crossing point for the second flutter mode is observable on Fig. 13. This alignment confirms the validity of a 2% structural damping assumption for the aluminum-construction Mod II aircraft. Furthermore, if only GVT-measured damping results are used (potentially a less conservative assumption due to uncertainty associated with damping measuring during GVT), the second flutter mode becomes the only critical flutter mode for the Mod II aircraft, with a flutter margin of ~100% relative to V_{NE}.

Visual illustrations of the aeroelastic mode shapes predicted by ZAERO are provided in Fig. 14. The first flutter mechanism involves stabilator rotation interacting with empennage porpoising (this empennage porpoising is coincident with, and most easily observed in the symmetric fore-aft movement of the wing). The second flutter mechanism, another empennage flutter, involves stabilator rotation interacting with vertical bending of the fuselage that drives vertical empennage and symmetrical first stabilator bending. The visual illustrations support the MPF values presented in Table 2.

Given that the NASA-STD-5002-required cross-orthogonality for significant modes was not achieved with the Mod II FEM correlation, a follow-on effort to verify the aircraft FEM was undertaken. Starting with the Mod II FEM, a regression FEM of the NASA best estimate of the P2006T was built referencing Tecnam technical documentation. The ZAERO flutter analysis using the NASA P2006T FEM yielded results consistent with a certified aircraft - a hump-mode interaction between stabilator rotation and empennage porpoising was predicted, but no instability occurred even for simulations up to 400 KEAS at Mach 0.6. Compared to a maximum-weight stock Tecnam P2006T airplane, the X-57 Mod II aircraft was heavier by ~150 lb. The additional mass was concentrated in the fuselage due to powertrain battery placement. The Mod II wing, however, was ~100 lb lighter than a stock P2006T wing because of the conversion from gasoline-powered engines to electric engines. This large ~250 lb relative mass change between the wing and fuselage on the Mod II aircraft lowered the empennage porpoising mode frequency. As a result, the Mod II aircraft was predicted to have comparatively adverse flutter characteristics relative to a stock P2006T airplane; however, even with this shift, the X-57 Mod II aircraft was predicted to have sufficient flutter margin for the planned flight-test envelope.

B. Mod III ZAERO Flutter Predictions

The Mod III aircraft unsteady aerodynamic models employed for the ZAERO flutter analysis are depicted in Fig. 15. Once again, body-type aerodynamic panel elements were used to model the fuselage, noseboom, and wingtip motor outer mold lines, and flat-plate type aerodynamic panel elements were used to model the wing, tail, HL motor pylons, and control surfaces. Two configurations of the unsteady aerodynamic model were explored: one with flaps deployed (5543 panel elements, shown in Fig. 15(a)), and the other with flaps stowed (6039 panel elements, shown in Fig. 15(b)). Aerodynamic paneling differences in the wing-flap connection between the two configurations are

illustrated in Fig. 15(c) (flaps-deployed) and Fig. 15(d) (flaps-stowed). In the flaps-stowed aerodynamic model, the wing and flap panels are smoothly connected across the hinge.

ZAERO matched point flutter analyses across Mach numbers 0.2 to 0.5 using the G-method flutter solution [8] for the Mod III configuration was completed with AIC matrices generated at 17 reduced frequencies. Again, the flutter analysis for Mod III included 60 natural FEM modes, following recommended practice for solution convergence. Significant modes of the Mod III aircraft as determined by ZAERO flutter analysis are highlighted in Table 4. Figure 16 shows the V-g curves from ZAERO simulations at Mach 0.4 for flaps-deployed and flaps-stowed conditions. The ZAERO input included no structural damping (since no Mod III aircraft GVT was performed), therefore 0% and 2% damping crossings are employed to determine flutter speeds. The blue and red lines in the Fig. 16 V-g plots illustrate the first and second flutter modes, respectively. Both flutter modes exhibit catastrophic instability and cross the 2% damping boundary as speed increases. Predicted flutter speeds and frequencies for first two flutter mechanisms of Mod III with flaps deployed and flaps stowed are presented in Table 5. The resulting predicted flutter boundaries are shown on the X-57 project flight envelope (Fig. 17). The lowest flutter speed predicted for the Mod III aircraft at the 2% damping boundary is 288 KEAS, and the predicted flutter margin is ~65% relative to V_{NE}. Change in predicted flutter speed as a result of flap deployment was minimal, as shown by the closely spaced blue and green lines on Fig. 17. Variances were < 2% for the first flutter mode and < 1% for the second flutter mode.

Illustrations of the first and second flutter mode shapes predicted by ZAERO are presented in Fig. 18. The first flutter mechanism demonstrates classical anti-symmetric wing bending and torsion and occurs at ~13.5 Hz (Table 5). The second flutter mechanism is an empennage flutter which occurs at ~19.6 Hz (Table 5), and involves stabilator rotation, vertical bending of the fuselage that drives vertical empennage motion, and stabilator bending. The wing/wingtip cruise motor junction area acts as a nodal line for the second flutter mode. Modal participation factors at Mod III-predicted flutter crossings predicted are presented in Table 6, and support the visual illustrations of the flutter mode shapes.

For Mod III, a third flutter mode driven by the wing symmetrical torsion FEM mode (Mode 13, Table 4) is depicted by a black line in Fig. 16. This mechanism is predicted to cross the 2% damping boundary at > 380 KEAS. Few details of this flutter mechanism are presented since it is predicted to occur at even higher speeds than the first two mechanisms and is unique to the Mod III configuration.

C. Mod IV ZAERO Flutter Predictions

Mod IV aircraft unsteady aerodynamic models employed for ZAERO flutter analysis (depicted in Fig. 19) were developed from the Mod III aerodynamic models by adding body-type panel elements to represent the HL motor outer mold lines. ZAERO unsteady aerodynamic simulations for both flaps-deployed (6205 panel elements) and flaps-stowed (6627 panel elements) conditions utilized AIC matrices generated at 17 reduced frequencies. Flutter analysis was performed across Mach numbers 0.3 to 0.5. The Mod IV flutter analyses included 80 natural FEM modes following the recommended practice for solution convergence of including FEM modes up to 3 times the frequency at which flutter is predicted. While flutter is predicted at similar frequencies across the Mod II, III, and IV configurations (17-20 Hz), the addition of HL motors results in many more structural modes in the Mod IV FEM. Significant modes of the Mod IV aircraft as determined by ZAERO flutter analysis are highlighted in Table 4. Figure 20 presents the V-g curves from ZAERO simulations at Mach 0.4. A list of predicted flutter speeds and frequencies for the Mod IV aircraft are presented in Table 7, and flutter boundaries on the flight envelope are shown in Fig. 21. When assuming 2% structural damping for the Mod IV aircraft, the predicted flutter margin is > 80% relative to V_{NE}. Change in predicted flutter speed due to flap deployment was minimal, as shown by the closely spaced blue and green lines on Fig. 21. Illustrations of the predicted first and second flutter mode shapes of the Mod IV aircraft are presented in Fig. 22.

The Mod III classical wing bending and torsion flutter mechanism (blue V-g line in Fig. 16, and flutter mode shape in Fig. 18(a)) is no longer present in the Mod IV configuration (Fig. 20). The addition of distributed HL motors along the wingspan alters the torsional stiffness of the Mod IV wing. Flutter analysis predicts the shift in antisymmetric wing torsion mode frequency (Table 4) and aerodynamic load changes induced by the HL nacelles attached near the wing bottom surface, passively suppress wing bending-torsion flutter for the Mod IV aircraft. A front-view illustration of the ZAERO aerodynamic model differences between Mod III and Mod IV is presented in Fig. 23. Comparing Mod III and Mod IV flutter boundaries on the flight envelope plots (Fig. 17 versus Fig. 21) shows the Mod III configuration is predicted to encounter flutter at a lower speed, and supports the conclusion that having only the large wingtip motors results in adverse classical flutter characteristics.

The Mod IV first flutter mechanism is an empennage flutter which occurs at ~19.3 Hz (Table 7), and involves stabilator rotation, vertical bending of the fuselage that drives vertical empennage motion, and stabilator bending. The Mod IV first flutter mode shape (illustrated in Fig. 22(a)) is supported by the MPFs presented in Table 8. Empennage

flutter driven by stabilator rotation, stabilator bending, and vertical empennage movement is predicted across the Mod II, III, and IV aircraft configurations. The associated flutter speeds and frequencies for empennage flutter across the X-57 configurations are presented in Table 9. As aircraft weight increases, the predicted speed at which empennage flutter occurs and the frequency of the empennage flutter mode both decrease.

The second predicted Mod IV flutter mechanism occurs at ~46 Hz (Table 7) and involves flap and wing torsion modes. Although the wing FEM was not well correlated at these frequencies, the second flutter mode may not be problematic for the Mod IV aircraft due to a few factors. ZAERO panel methods cannot accurately model the aerodynamics of a deployed flap. During the Mod III wing GVT, measured damping values of control surface modes were 4-8 times larger than those of wing modes. Additionally, based on aircraft flight experience, external flow over aerodynamic surfaces typically does not excite structural modes at higher frequencies. For these reasons, ZAERO may be overpredicting aeroelastic response of the flap mode.

V. FUN3D Flutter Predictions

The NASA FUN3D software [9] was used to perform CFD aeroelastic simulations of the Mod III and Mod IV aircraft configurations to augment the ZAERO results. FUN3D is a finite-volume, unstructured-grid, node-based, mixed-element Reynolds-averaged Navier–Stokes (RANS) flow solver. Given the subsonic flight speeds of the X-57 aircraft, it was determined that ZAERO was sufficient for predicting wing and tail mechanism aeroelastic instabilities. ZAERO, however, employs panel-method aerodynamics, so it is unable to capture instabilities driven by in-plane motion of aerodynamic surfaces. For the Mod III/IV aircraft, FUN3D helped fill in the gaps for any potential flutter mechanisms of the long-span, narrow-chord flaps driven by their fore-aft or lateral movement. The deployed-flap full-aircraft FEMs previously used for the Mod III/IV ZAERO analysis were utilized with FUN3D. Structural modes were obtained by way of normal modes analysis (SOL103) using MSC NASTRAN. The Mod III CFD aeroelastic analysis included 182 flexible modes, and the Mod IV CFD aeroelastic analysis included 200 flexible modes to capture higher frequency flap, aileron, and motor nacelle modes. The aerodynamically converged fine-resolution full-span tetrahedral Mod III and Mod IV CFD grids contained 32 million and 65 million nodes, respectively. Images of these CFD grids are presented in Fig. 24.

The workflow for computing aeroelastic stability using FUN3D is briefly summarized below. Greater detail on the FUN3D aeroelastic workflow and specific computation methods utilized can be found in papers by Massey et. al [10-12], and Chwalowski et. al. [13]. As a pre-processing step, FEM structural mode shapes were interpolated onto the CFD mesh using radial basis functions [14]. An example image of the FEM nodes used for shape projection during interpolation is shown in Fig. 25(a), and a resulting CFD grid deformation is shown in Fig. 25(b). Then, aeroelastic stability with FUN3D was assessed using the following steps:

1) First a steady RANS solution was computed on the rigid aircraft at a prescribed flight condition using only the CFD grid.
2) A static aeroelastic solution was obtained by continuing the CFD simulation in a time-accurate unsteady mode and allowing the structure to deform, but with high structural damping so the structure reached an equilibrium position with respect to the mean flow (this is sometimes referred to as the critically-damped solution).
   - For the Mod III/IV simulation a structural damping of 0.999 was used.
   - The displacement versus time is shown in Fig. 25(c), during the time from 0 to 0.5 s.
3) Dynamic aeroelastic response was calculated by setting structural damping to 0 and perturbing the structure in generalized velocity for each mode included in the structural model, and then restarting the time-accurate unsteady flow solution.
   - A displacement-versus-time example is shown in Fig. 25(c), during the time after 0.5 s.
   - At the start of Step 3, an alternative approach would have been to set the structural damping ratio to 0.02 (i.e. assuming 2% structural damping)
4) Damping for each mode was estimated using the matrix pencil method [15] and all modal responses were examined.
   - An example annotation is shown in the upper left corner of the Fig. 25(c) plot.

To find the predicted aeroelastic boundary, a starting flight condition of Mach 0.28 at 2200 ft was specified for the Mod III and Mod IV simulations. Additional CFD aeroelastic analyses at increasing Mach numbers were performed until unstable modes were predicted. For the Mod III aircraft, flap mode instability was predicted at Mach 0.35/222 KEAS. For the Mod IV aircraft, flap mode instability was predicted at Mach 0.47/300 KEAS. It is possible that for the Mod IV configuration, the additional flap lateral brackets which are part of the HL motor/wing attachment hardware, provided additional stiffness to flap mechanisms, and delay the airspeed at which flap mode instability

occurs in FUN3D simulations. For both Mod III and Mod IV, flap instabilities were predicted to occur only at speeds greater than the prescribed maximum flap deployment airspeed of 132 KCAS. These FUN3D predictions are consistent with the ZAERO predictions of flap flutter occurring above airspeeds at which flaps would be used.

A limitation of CFD aeroelastic simulations is that once an instability grows large enough that local grid deformations exceed the capability of the mesh, the simulation terminates; therefore, it may be difficult to determine the modes involved in the predicted flutter mechanism. An example of this from the Mod III aeroelastic simulation at Mach 0.4 is presented in Fig. 26. A flap mode instability (Mode 37) grows to the point where the mesh becomes invalid. Modes 16 (wing torsion) and 12 (wing bending w / empennage roll) were predicted to be the primary participants in the first flutter mode by the Mod III ZAERO flutter analysis (Table 6). Mode 15 (stabilator rotation), however, has a larger negative damping value for the Mod III aircraft than Mode 12. The ZAERO flutter analysis predicted Mode 15 to be a primary flutter participant in the second Mod III flutter mode (Table 6), rather than the first flutter mode encountered at lower airspeed. Computational fluid dynamics aeroelastic techniques such as the linearized frequency-domain (LFD) approach implemented in FUN3D, and AeroElastic Reduced-Order Modeling (AEROM) developed by NASA Langley Research Center, can be used to better determine which modes contribute to flutter in a particular CFD-based aeroelastic solution [16]. However, such techniques were not utilized during this effort.

VI. Implications for Flight-test Planning

Predicted flutter boundaries help inform flight-test planning. When high flutter margins are predicted against aircraft V_{NE} and confidence in models is high, flight-testing can be performed without real-time monitoring of aircraft structural dynamic modes. When margins are lower or confidence in FEMs or aeroelastic predictions is low, real-time monitoring of aircraft structural dynamic modes is required.

The NASA AFRC guidance is to maintain a 15% flutter margin (on both equivalent airspeed and Mach number) when both structural and aerodynamic models have been aeroelastically validated [17]. If only the structural model is validated, a higher flutter margin of 30-40% is recommended [17]. In the case of the Mod II FEM, which did not meet the NASA-STD-5002 requirements specified for significant modes, a relatively high 50-60% airspeed margin was recommend for Mod II flights. This meant, when using 2% structural damping Mod II ZAERO predictions, only flight-test points below 177 KEAS could be flown without real-time accelerometer instrumentation measuring primary flutter participant modes. If there were high confidence in GVT-measured structural damping values, however, GVT-measured damping ZAERO predictions would allow flying test points out to 211 KEAS without instrumentation. These airspeed limits would not have needed to remain fixed throughout the X-57 Mod II flight-test campaign. Most likely, after some aeroelastic validation data were gathered using flight accelerometers during early flight tests, airspeed limits from predicted flutter margins could have been relaxed.

In the absence of GVT correlation of the FEM, an even higher airspeed margin of 100% is recommended. This recommendation carries a caveat that there is confidence that the aircraft structural dynamics are adequately captured in the aeroelastic predictions. In a hypothetical scenario of Mod III/IV flight-testing without conducting a GVT of the full aircraft, the current FEM models could allow for flight up to 100% of the predicted boundary. This determination might be based on the rationale that the Mod III wing FEM was well correlated, Mod II flight tests provided aeroelastic validation data for the fuselage and empennage models, and FEM/flutter analysis was performed by experienced practitioners and results were thoroughly peer reviewed. In this scenario, test planning could allow for Mod III aircraft flight up to 146 KEAS, and for Mod IV aircraft flight up to 159 KEAS, when using 2% structural damping ZAERO predictions.

VII. Conclusions

Flutter analysis for X-57 “Maxwell” project was performed using finite element models (FEMs) correlated against Mod II aircraft ground vibration test (GVT) and Mod III wing GVT data. Based on the results, no restriction of the Mod II aircraft flight-test envelope was planned. The X-57 aircraft was instrumented with accelerometers for real-time monitoring of the Mod II primary flutter participant modes. The Mod II first flutter mechanism was predicted to be the stabilator rotation mode coupling with empennage porpoising mode. The Mod III first flutter mechanism was predicted to be a typical wing bending-torsion behavior resulting from the structural dynamics of the large electric motors located at the wingtips. For the Mod IV configuration, addition of distributed high-lift motor masses along the wingspan suppressed the bending-torsion behavior predicted for the Mod III wing. The Mod IV configuration first flutter mechanism was predicted to be empennage flutter. This empennage flutter mechanism was also predicted for the Mod II and III aircraft, but as the second flutter mechanism (occurring at higher speeds than the first flutter). Predicted empennage flutter was driven by stabilator rotation, vertical empennage motion, and stabilator bending

modes, and its presence across the Mod II, III, and IV aircraft configuration is consistent with the fuselage and empennage FEM being reused across X-57 aircraft configuration models. Aeroelastic computational fluid dynamics simulations of the Mod III/IV aircraft predicted flap mode instability, but at speeds outside the flap deployment envelope. All aeroelastic instability boundaries were predicted to have a margin of greater than 60 percent over the never-exceed or maximum-flaps-extended airspeeds.

Acknowledgements

The detailed finite element modeling of the X-57 aircraft would not have been possible without the incredible support received from Costruzioni Aeronautiche Tecnam (Capua, Italy) and Fabio Russo (the Tecnam Chief of Research & Development and Product Development). We thank them sincerely for their help throughout all phases of the X-57 project.

References

[1] National Aeronautics and Space Administration, "X-57 Maxwell," Fact Sheet, https://www.nasa.gov/centers/armstrong/news/FactSheets/FS-109.html [retrieved June 12, 2024].

[2] Borer, N. K., Guether, S. C., Litherland, B. L., and Kohlman, L., "Design and Performance of a Hybrid-Electric Fuel Cell Flight Demonstration Concept," AIAA Paper 2018-3357, June 2018. doi: 10.2514/6.2018-3357

[3] ZONA Technology, Inc., *ZAERO User's Manual Version 9.3,* ZONA Technology, Inc., Scottsdale, Arizona, 2019.

[4] Heeg, J., Stanford, B. K., Wieseman, C. D., Massey, S. J., Moore, J., Truax, R., and Miller, K. "Status Report on Aeroelasticity in the Vehicle Development for X-57 Maxwell," AIAA Paper 2018-3487, June 2018. doi: 10.2514/6.2018-3487

[5] Spivey, N., Truong, S., and Truax, R., "All-Electric X-Plane, X-57 Mod II Ground Vibration Test," Edwards, CA, August 2020. Available at: https://www.nasa.gov/directorates/armd/x-57-technical-papers/ [retrieved June 12, 2024].

[6] National Aeronautics and Space Administration, "Load Analyses of Spacecraft and Payloads," Revision A, NASA-STD-5002A, September 2019.

[7] ATA Engineering, Inc., Attune Software webpage, https://www.ata-e.com/software/ata-software/attune/ [retrieved June 12, 2024].

[8] ZONA Technology, Inc., *ZAERO Theoretical Manual Version 9.3,* ZONA Technology, Inc., Scottsdale, Arizona, 2019.

[9] Biedron, R. T., et. al., *FUN3D Manual 13.7,* NASA/TM-20205010139 Corrected Copy, November 2020.

[10] Massey, S. J., and Chwalowski, P., "Computational Aeroelastic Analysis of Ares Crew Launch Vehicle Bi-Modal Loading," AIAA Paper 2010-4373, June 2010. doi: 10.2514/6.20104373

[11] Massey, S. J., Stanford, B. K., Wieseman, C. D., and Heeg, J., "Aeroelastic Analysis of a Distributed Electric Propulsion Wing," AIAA Paper 2017-0413, January 2017. doi: 10.2514/6.20170413

[12] Massey, S. J., Stanford, B. K., and Jacobson, K. E., "Progress on Flutter Analysis of the X-56A for the Third Aeroelastic Prediction Workshop," AIAA Paper 2022-2315, January 2022. doi: 10.2514/6.20222315

[13] Chwalowski, P., Silva, W. A., Wieseman, C. D., and Heeg, J., "CFD Model Of The Transonic Dynamics Tunnel With Applications," STO-AVT-284, April 2018. Available at: https://ntrs.nasa.gov/citations/20180006304 [retrieved June 12, 2024].

[14] Massey, S. J., "Mode shape interpolation via radial basis functions," source code with documentation. Available at: https://github.com/nasa/rbf [retrieved June 12, 2024].

[15] Kiviaho, J. F., Jacobson, K. E., and Kennedy, G. J., "Flutter Boundary Identification from Time-Domain Simulations Using the Matrix Pencil Method," *AIAA Journal*, Vol. 57, No. 8, 2019, pp. 3639-3645. doi: 10.2514/1.J058072

[16] Waite, J. M., Bartels, R. E, Stanford, B. K., "Aeroelastic Model Development for the Integrated Adaptive Wing Technology Maturation Project Wind-Tunnel Test," AIAA Paper 2020-2717, June 2020. doi: 10.2514/6.2020-2717

[17] National Aeronautics and Space Administration, "Aircraft Structural Safety of Flight Guidelines," AFG-7123.1-001, Rev A-1, May 2021.

Tables

Table 1. Summary of the X-57 Mod II aircraft final finite element model modes and ground vibration test-measured damping [5] (significant modes of first two flutter mechanisms presented in Table 2 and highlighted in orange).

Mode	Frequency, Hz	Measured damping, %		Description
		ζ (GVT)	$g = 2\zeta$	
1~6	0.0			Rigid body modes
7	8.44	0.57	1.14	Wing 1st bending
12	14.15	0.44	0.88	Stabilator rotation
14	17.18	1.24	2.48	Wing 1st torsion
15	17.34	0.95	1.90	Stabilator roll, Vertical Tail 1st bending
16	17.58	1.43	2.86	Empennage porpoising, coincident w/ wing fore-aft
18	20.72	1.31	2.62	Fuselage vertical 1st bending, stabilator 1st bending

Table 2. The ZAERO-predicted modal participation factors at flutter crossing of the X-57 Mod II aircraft at Mach 0.3.

Mode	Frequency, Hz	First flutter		Second flutter	
		Rank	MPF, % [sum]	Rank	MPF, % [sum]
1~6	0.00	6	3.09 [93.7]	6	2.21 [91.0]
7	8.44	8	0.96 [96.8]	4	3.60 [85.9]
12	14.15	2	27.8 [73.4]	1	35.9 [35.9]
14	17.18	7	2.23 [95.9]	9	0.96 [95.1]
15	17.34	3	6.19 [79.6]		
16	17.58	1	45.6 [45.6]	5	2.83 [88.8]
18	20.72	4	5.50 [85.1]	2	32.5 [68.4]
42	41.14	5	5.47 [90.6]	3	13.9 [82.3]

Table 3. The ZAERO-predicted flutter speeds and frequencies of the X-57 Mod II aircraft.

Flutter mode	Mach	0% damping (from Fig. 11)		2% damping (from Fig. 11)		GVT-measured damping (from Fig. 12)	
		Speed, KEAS	Freq, Hz	Speed, KEAS	Freq, Hz	Speed, KEAS	Freq, Hz
1	0.2	217.6	17.50			Not performed	
	0.3	199.2	17.49				
	0.4	190.7	17.49				
	0.5	185.0	17.49	283.5	17.55		
2	0.2					Not performed	
	0.3	409.3	19.73				
	0.4	345.9	19.64	386.6	19.74	387.3	19.72
	0.5	327.5	19.68	354.6	19.73	355.6	19.69
	0.6	Not performed				338.4	19.70

Table 4. Summary of the X-57 Mod III/IV aircraft modes predicted by finite element models (significant modes as determined by flutter analysis highlighted in orange).

Mod III		Mod IV		Description
Mode	Frequency, Hz	Mode	Frequency, Hz	
1~6	0.0	1~6	0.0	Rigid body modes
7	2.31	7	2.29	Wing 1st bending
10	7.69	10	7.56	Wing fore-aft
11	11.40			Stabilator roll w/ wing 2nd bending out-of-phase
		11	9.90	Wing 2nd bending, fuselage torsion
		12	11.45	Stabilator roll
12	11.60			Wing 2nd bending w/ stabilator roll in- phase, fuselage torsion
13	12.97	14	12.81	Wing torsion symmetric
		15	13.47	Wing torsion anti-symmetric, some empennage roll+yaw
14	13.57	16	13.55	Empennage yaw+roll, some wing torsion anti-symmetric
15	14.17	17	14.17	Stabilator rotation
16	14.23			Wing torsion anti-symmetric, empennage roll
22	20.03	20	19.95	Fuselage lateral bending, vertical tail bending
23	20.51	21	20.35	Fuselage vertical bending, stabilator bending
33	31.46	33	31.48	Stabilator vertical bending, empennage porpoising
45	41.11	44	41.14	Stabilator rotation (higher order), out-of-phase w/ stab mass balance

Table 5. The ZAERO-predicted flutter speeds and frequencies of the X-57 Mod III aircraft.

Flutter mode	Mach	Flap deployed				Flap stowed			
		0% damping		2% damping		0% damping		2% damping	
		Speed, KEAS	Freq, Hz	Speed, KEAS	Freq, Hz	Speed, KEAS	Freq, Hz	Speed, KEAS	Freq, Hz
1	0.3	250.4	13.70	307.2	13.51	254.2	13.71	314.5	13.52
	0.4	255.0	13.63	296.1	13.45	257.7	13.64	302.1	13.46
	0.5	258.2	13.55	287.9	13.39	257.4	13.58	293.9	13.41
2	0.3	349.4	19.48	434.6	19.72	349.9	19.50	433.6	19.72
	0.4	322.7	19.46	355.2	19.52	325.0	19.49	358.4	19.55
	0.5	308.8	19.48	332.0	19.51	311.6	19.51	335.6	19.54

Table 6. The ZAERO-predicted modal participation factors at 1st flutter crossing of the X-57 Mod III aircraft at Mach 0.3.

Mode	Freq, Hz	Flap stowed					Flap deployed				
		1st flutter mode		2nd flutter mode			1st flutter mode		2nd flutter mode		
		Rank	MPF, % [sum]	Rank	MPF, % [sum]		Rank	MPF, % [sum]	Rank	MPF, % [sum]	
1				4	1.18	4.56 [86.4]			4	1.16	4.54 [86.3]
3					1.31					1.33	
4	0.00	5	2.57 [95.2]				5	2.64 [95.3]			
5					2.07					2.05	
11	11.40	3	6.49 [86.4]				4	5.73 [92.6]			
12	11.60	2	14.3 [79.9]				2	14.8 [80.5]			
14	13.57	4	6.23 [92.6]				3	6.36 [86.9]			
15	14.17			1	36.1 [36.1]				1	35.3 [35.3]	
16	14.23	1	65.6 [65.6]				1	65.8 [65.8]			
22	20.03			5	3.53 [90.0]				5	3.15 [89.5]	
23	20.51			2	33.0 [69.1]				2	33.7 [69.0]	
33	31.46			6	3.01 [93.0]				6	3.01 [92.5]	
45	41.11			3	12.9 [81.9]				3	12.7 [81.8]	

Table 7. The ZAERO-predicted flutter speeds and frequencies of the X-57 Mod IV aircraft.

Flutter mode	Mach	Flap deployed				Flap stowed			
		0% damping		2% damping		0% damping		2% damping	
		Speed, KEAS	Freq, Hz	Speed, KEAS	Freq, Hz	Speed, KEAS	Freq, Hz	Speed, KEAS	Freq, Hz
1	0.3	333.7	19.35	404.8	19.54	332.8	19.36	402.7	19.53
	0.4	309.5	19.35	340.3	19.40	309.5	19.35	340.4	19.40
	0.5	297.0	19.37	319.4	19.39	297.2	19.37	319.7	19.39
2	0.3	340.9	46.53	-	-				
	0.4	325.3	46.45	395.6	46.43				
	0.5	308.9	46.25	367.0	46.23				

Table 8. The ZAERO-predicted modal participation factors at 1st flutter crossing of the X-57 Mod IV aircraft at Mach 0.3.

Mode	Frequency, Hz	MPF, % [cumulative sum of MPF]	Ranking
1, 3, & 5	0.0	4.9 [87.1]	4
17	14.17	36.6 [36.6]	1
20	19.95	4.5 [91.6]	5
21	20.35	33.0 [69.7]	2
33	31.48	2.4 [94.1]	6
44	41.14	12.6 [82.3]	3

Table 9. The X-57 Mod II, III, and IV predictions for empennage flutter mode assuming 2% structural damping (stowed flaps conditions for Mod III and IV).

Mach	Flutter speed, KEAS			Flutter frequency, Hz		
	Mod II	Mod III	Mod IV	Mod II	Mod III	Mod IV
0.3	–	433.6	402.7	–	19.72	19.53
0.4	386.6	358.4	340.4	19.74	19.55	19.40
0.5	354.6	335.6	319.7	19.73	19.54	19.39

Figures

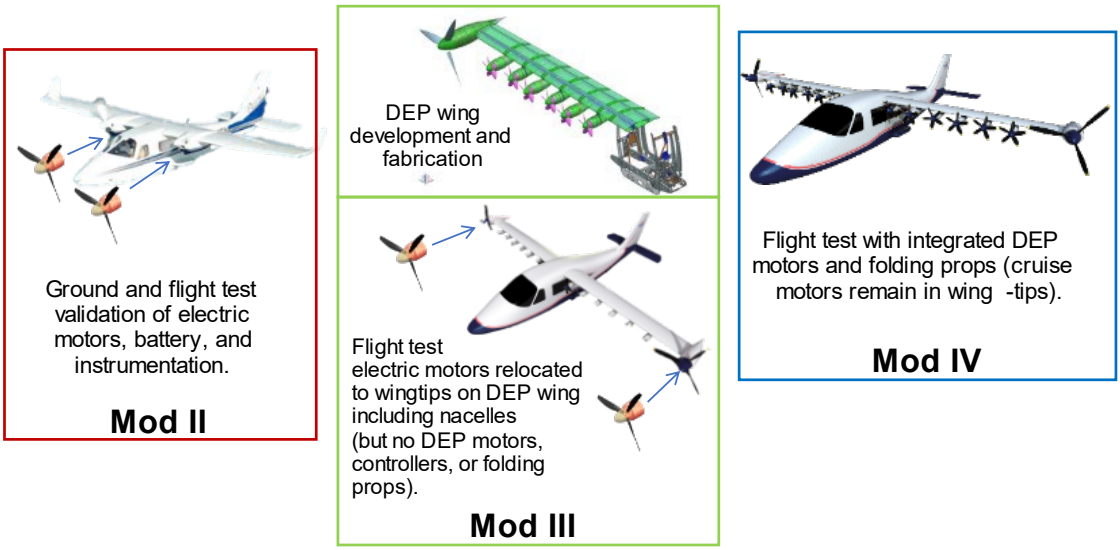

Fig. 1 Illustrations of the X-57 Mod II, III, and IV aircraft configurations.

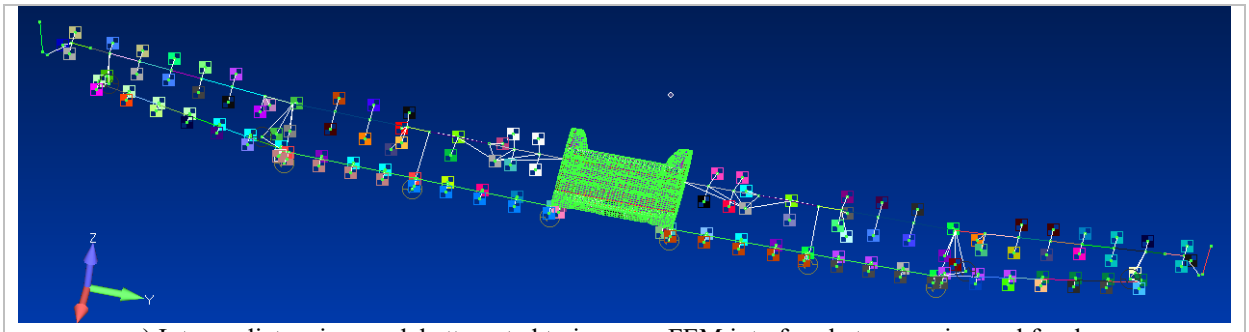

a) Intermediate wing model attempted to improve FEM interface between wing and fuselage

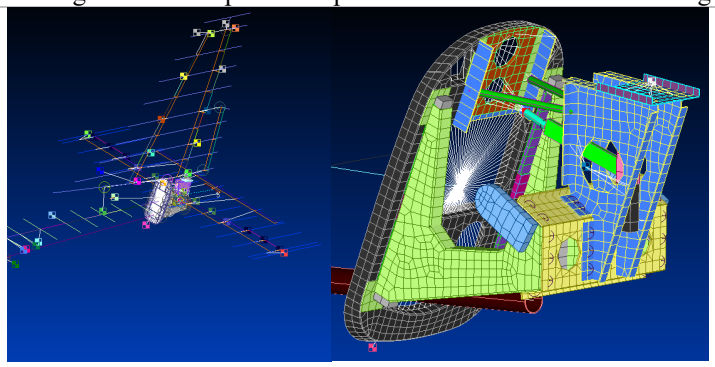

b) Intermediate FEM of interface between stabilator and aft fuselage

Fig. 2 Structural interfaces that were difficult to model using only beam elements in the Mod II finite element model.

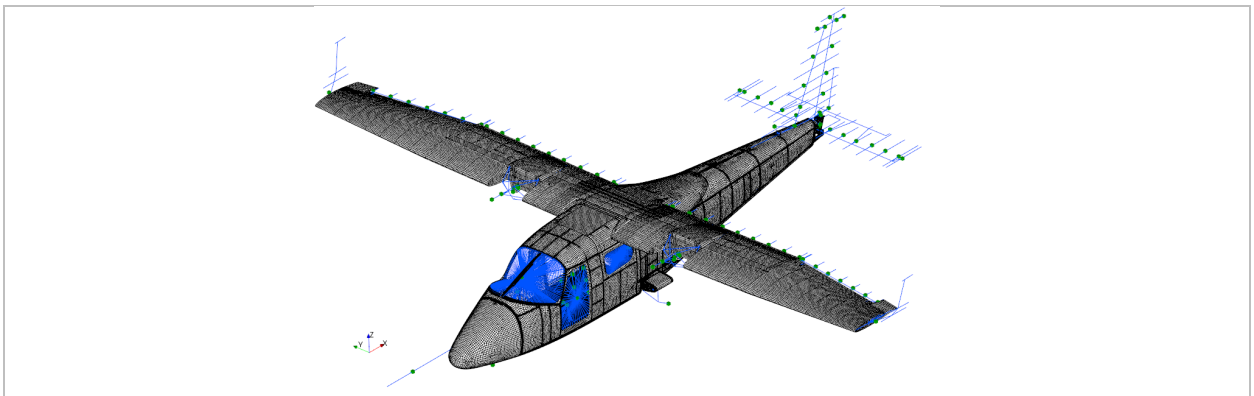

a) Isometric view of Mod II aircraft FEM

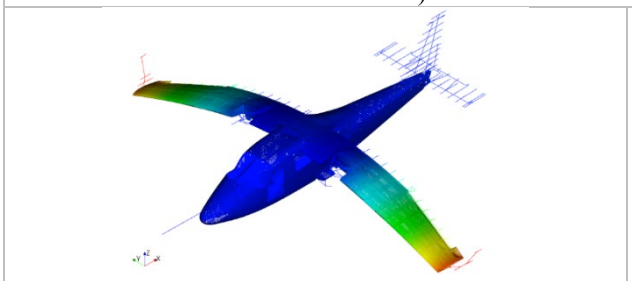

b) Mode 7, 8.44 Hz, Wing 1st bending

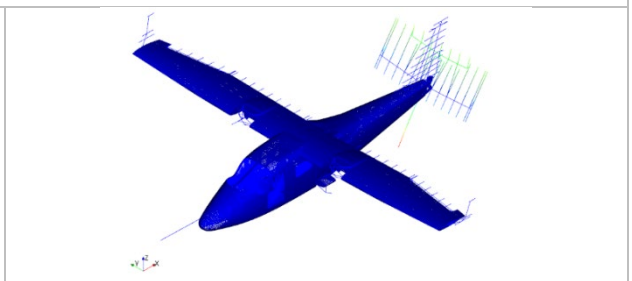

c) Mode 12, 14.15 Hz, Stabilator rotation

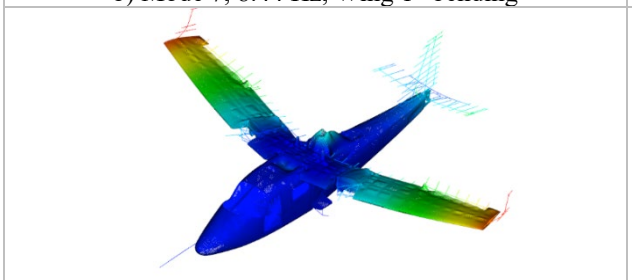

d) Mode 16, 17.58 Hz, Empennage porpoising coincident with w/ Wing fore-aft

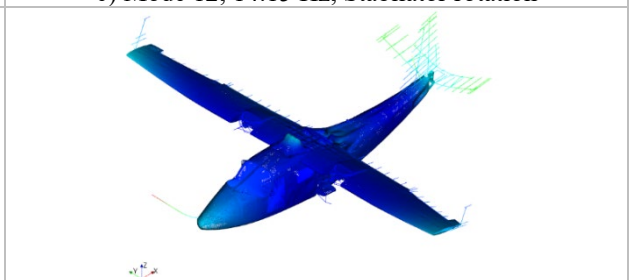

e) Mode 18, 20.72 Hz, Fuselage 1st bending w/ Stabilator 1st bending

Fig. 3 The final finite element model (FEM) of the Mod II aircraft, and illustrations of significant mode shapes.

			FEM Shapes																		Freq
			7	8	9	10	11	12	13	14	15	16	17	18	19	20	21	22	23	24	Pct
Otg	Test Shapes		8.46	8.87	10.97	12.27	14.10	14.15	16.09	17.26	17.61	17.68	18.78	20.77	22.55	23.89	25.11	25.63	26.21	26.68	Diff
100	1	7.83	99																		7.9
95	2	9.09		94								23									-2.4
90	3	10.36		15	92	37															5.9
85	4	11.49			35	90	25						28								6.7
80	5	12.14					24		15	44			30				20				42.2
75	6	13.68					98						21								3.1
70	7	14.17					27	92						31							-0.1
65	8	14.84							99												8.5
60	9	15.93			17	23	24			90			61								8.3
55	10	16.75								27	95										5.1
50	11	16.95		18	17	22			16	67	18		82		25						10.7
45	12	17.53						15				97		16							0.9
40	13	19.11						23				26		95				20			8.7
35	14	20.01						92						32							-29.3
30	15	20.69					18		15				31		95						9.0
25	16	21.39													58	25	67	16	38		17.4
20	17	21.95		22			35			19			30				68	19	56		14.4
15	18	24.55												32				23		24	-15.4
10	19	24.78				15										82	26		41	18	-3.6
5	20	26.38												15		26		45	46	75	1.1
0	21	27.25																58	40		-5.9

Fig. 4 Cross-orthogonality value comparison for the final Mod II finite element model and ground vibration test mode shapes.

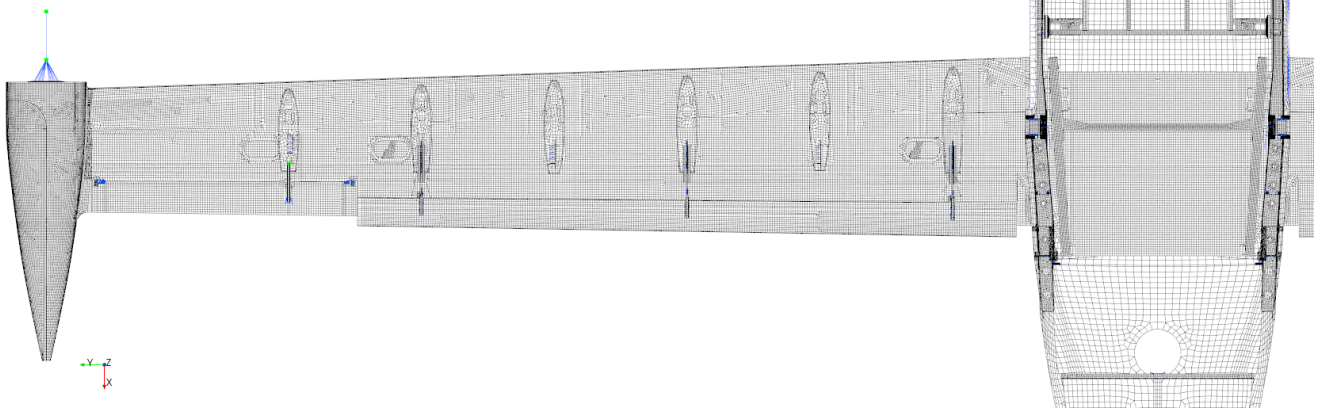

a) View of Mod III right wing from below showing H-frame fuselage attachment, and flap deployed

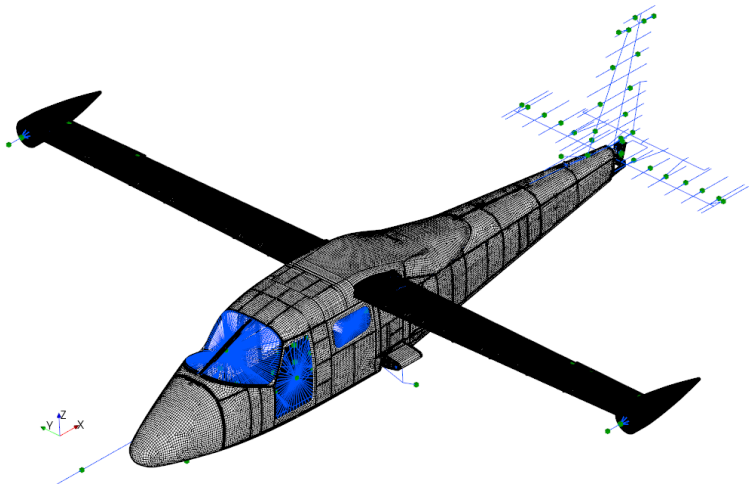

b) Isometric view of Mod III aircraft FEM

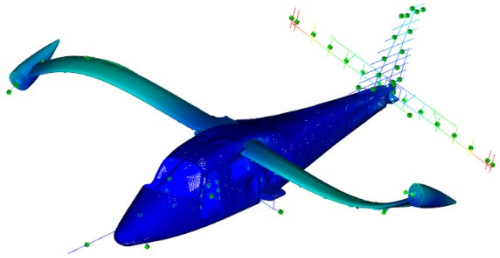

c) Mode 12, wing 2nd bending w/ stab roll

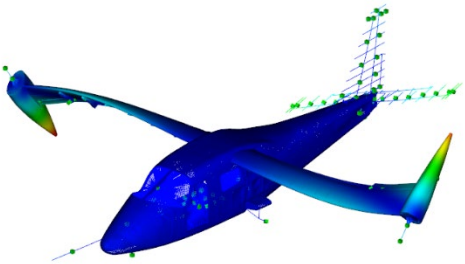

d) Mode 16, wing torsion anti-sym

Fig. 5 Images of the Mod III finite element model and significant mode shapes.

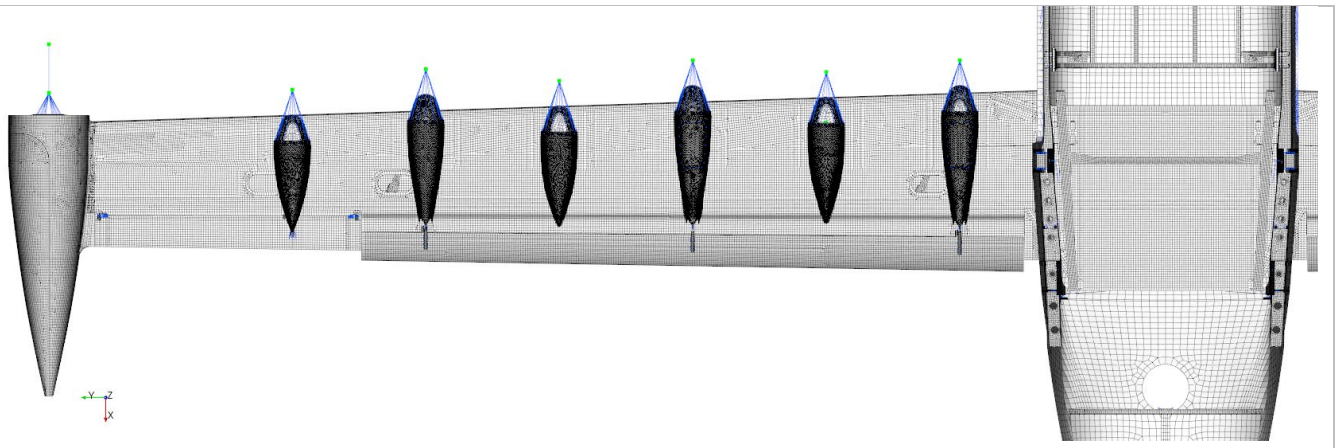

a) View of Mod IV right wing from below showing HL nacelles, H-frame fuselage attachment points, and flap deployed

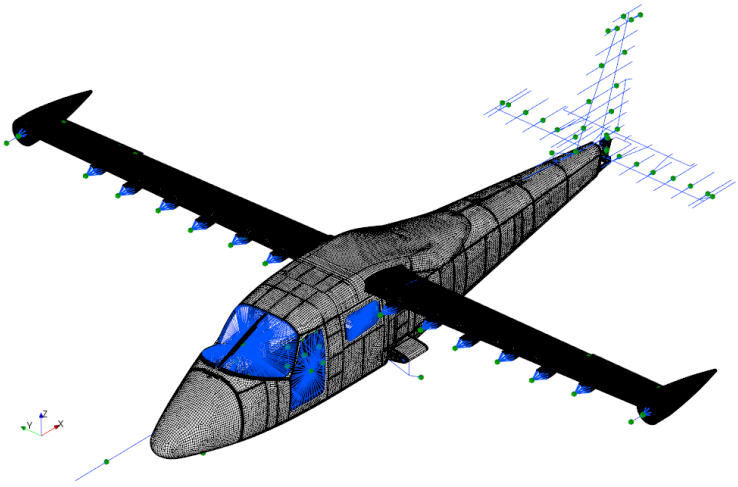

b) Isometric view of Mod IV aircraft FEM

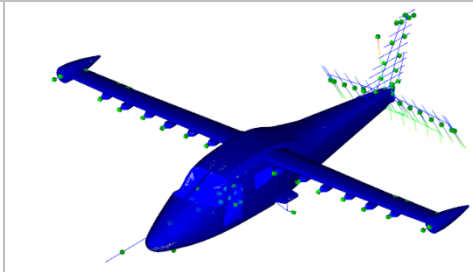

c) Mode 17, stabilator rotation

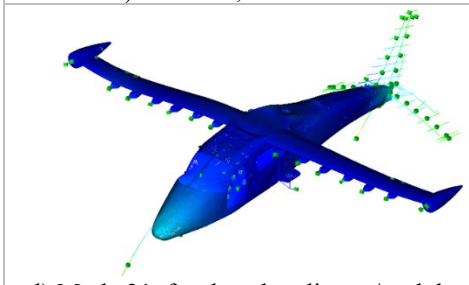

d) Mode 21, fuselage bending w/ stab bending

Fig. 6 Images of the Mod IV finite element model and significant mode shapes.

			FEM Shapes																			Freq
			1	2	3	4	5	6	7	8	9	10	11	12	13	14	15	16	17	18	19	Pct
Otg	Test Shapes		2.22	2.41	6.00	8.12	15.61	17.04	18.81	20.22	24.45	25.12	37.50	42.86	44.91	45.57	46.50	50.10	52.97	56.91	60.87	Diff
100	1	2.13	100	5																		4.2
95	2	2.25		100																		7.1
90	3	6.21			100																	-3.3
85	4	7.88				100																3.0
80	5	14.82	5				99	7														5.3
75	6	15.77		7			6	99														8.0
70	7	22.78									99	5										7.3
65	8	23.34				6						99										7.6
60	9	36.16											95			5	5			6		3.7
55	10	40.89	6								5			36	87	20	13					9.8
50	11	41.35	9										7	37	19	87	6					10.2
45	12	42.30	6	8							5			25			91	11			6	9.9
40	13	44.26							17	13				80	10	27	40	23				-3.2
35	14	48.30								5				12		5	8	95	9			3.7
30	15	52.32												7		8			94		27	1.2
25	16	54.77	5	6			6	5				6	7			7				91		3.9
20	17	57.21		6															5	6	85	6.4
15	18	59.38	6	6			7				7										84	2.5

Fig. 7 Cross-orthogonality value comparison for the Mod III wing-only finite element model and ground vibration test mode shapes with the flaps in the stowed position.

			FEM Shapes																				Freq
			1	2	3	4	5	6	7	8	9	10	11	12	13	14	15	16	17	18	19	20	Pct
Otg	Test Shapes		2.23	2.43	6.01	8.14	15.44	16.84	17.29	18.33	24.44	25.16	34.36	34.49	39.35	42.37	43.56	45.52	49.55	53.72	54.77	59.10	Diff
100	1	2.15	100																				3.4
95	2	2.26	6	100																			7.4
90	3	6.00			100																		0.2
85	4	7.52				100																	8.3
80	5	14.74	5				100																4.8
75	6	15.63		7				99	6														7.7
70	7	17.45							99						9								-0.9
65	8	19.63								100													-6.7
60	9	22.81								5	99					6							7.1
55	10	23.37				5						99											7.7
50	11	30.57							6				96	12	5								12.4
45	12	32.58								9			11	96									5.9
40	13	34.11													96		10	13			7		15.4
35	14	38.43	6								5				12	65	68	18	6	5			13.3
30	15	40.79							5						8	41	10	86					11.6
25	16	43.99	5													70	61	14	32			10	-3.7
20	17	46.73	5						5						15	11		12	25	73	56		15.0
15	18	47.59									5					13	23	5	91	9	11	5	4.1
10	19	48.59	6		6						5					13	9	12	21	84	14	12	10.6
5	20	49.70	7					5			6					8	16	6	16	91	22		8.1
0	21	50.40		9			5					5			5			23			93		8.7
	22	56.34						7				6				5	13	9	15	14	12	81	4.9

Fig. 8 Cross-orthogonality value comparison for the Mod III wing-only finite element model and ground vibration test mode shapes with the flaps in the deployed position.

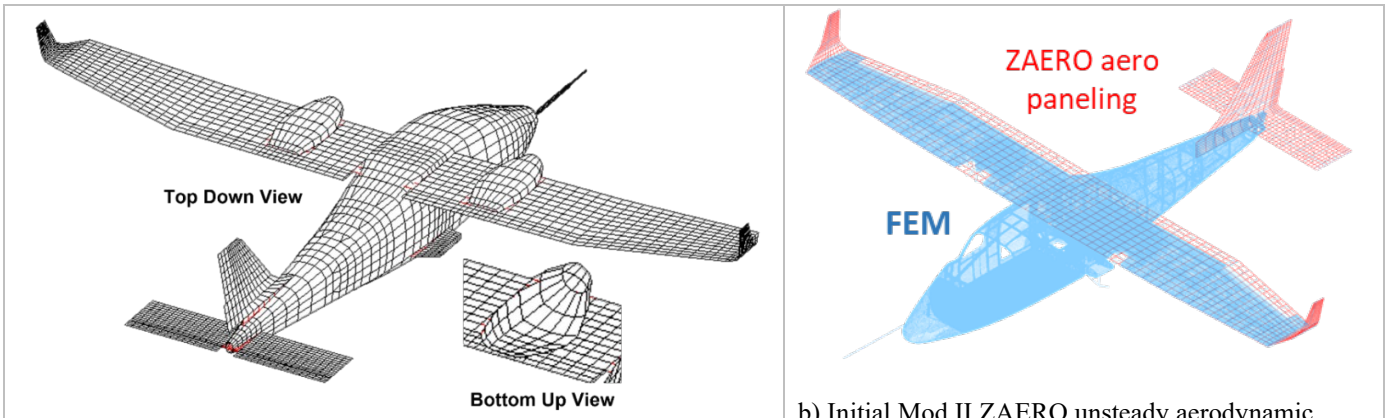

a) Final Mod II ZAERO unsteady aerodynamic model

b) Initial Mod II ZAERO unsteady aerodynamic model (in red) overlayed on Mod II FEM (in blue)

Fig. 9 The ZAERO unsteady aerodynamic models of the Mod II aircraft.

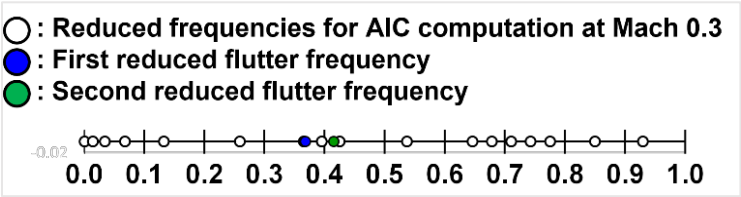

Fig. 10 The ZAERO-reduced frequencies for the flutter analysis of the Mod II aircraft.

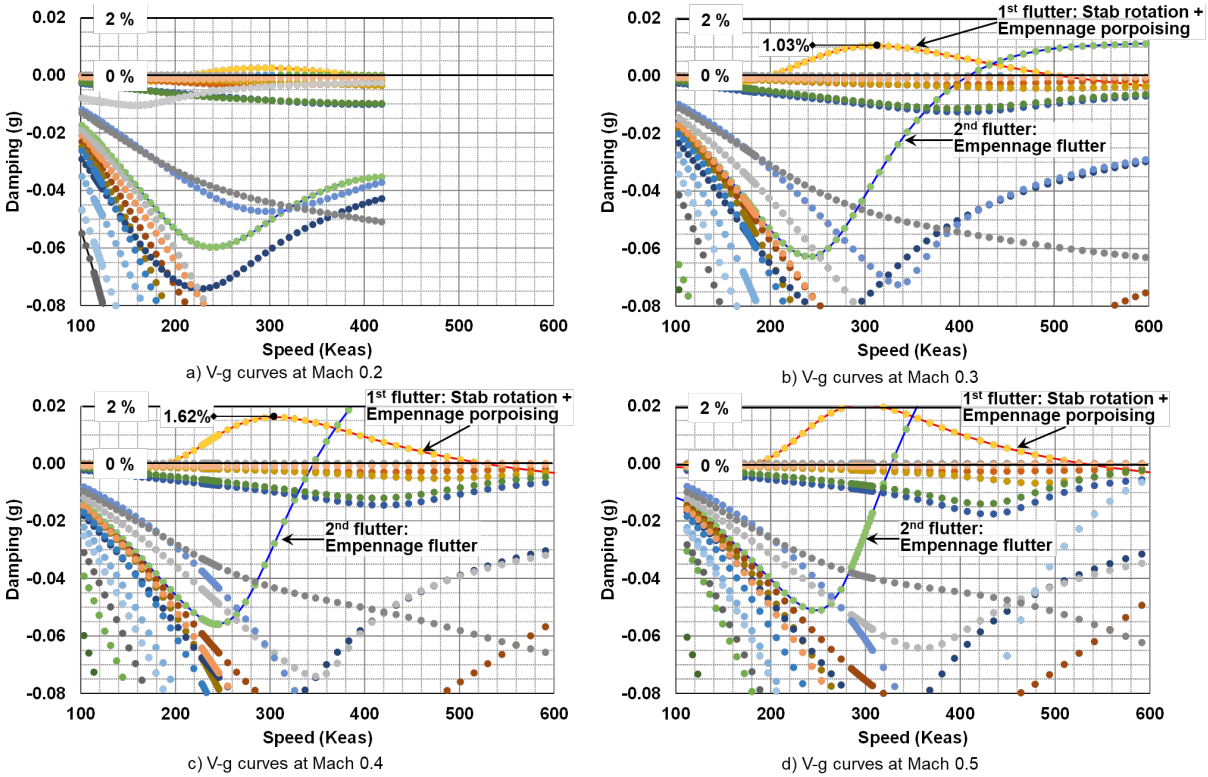

a) V-g curves at Mach 0.2

b) V-g curves at Mach 0.3

c) V-g curves at Mach 0.4

d) V-g curves at Mach 0.5

Fig. 11 The ZAERO-predicted V-g curves of the Mod II aircraft, using 0% and 2% damping crossings.

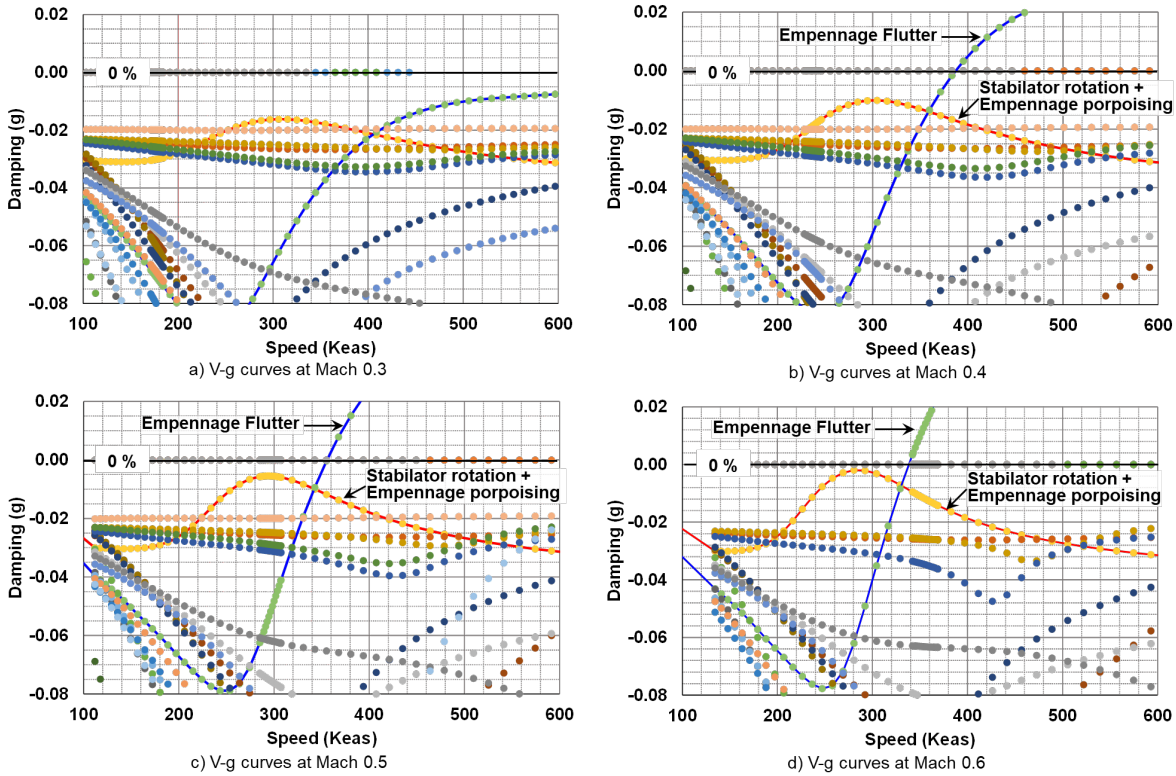

Fig. 12 The ZAERO-predicted V-g curves of the Mod II aircraft, using ground vibration test-measured damping.

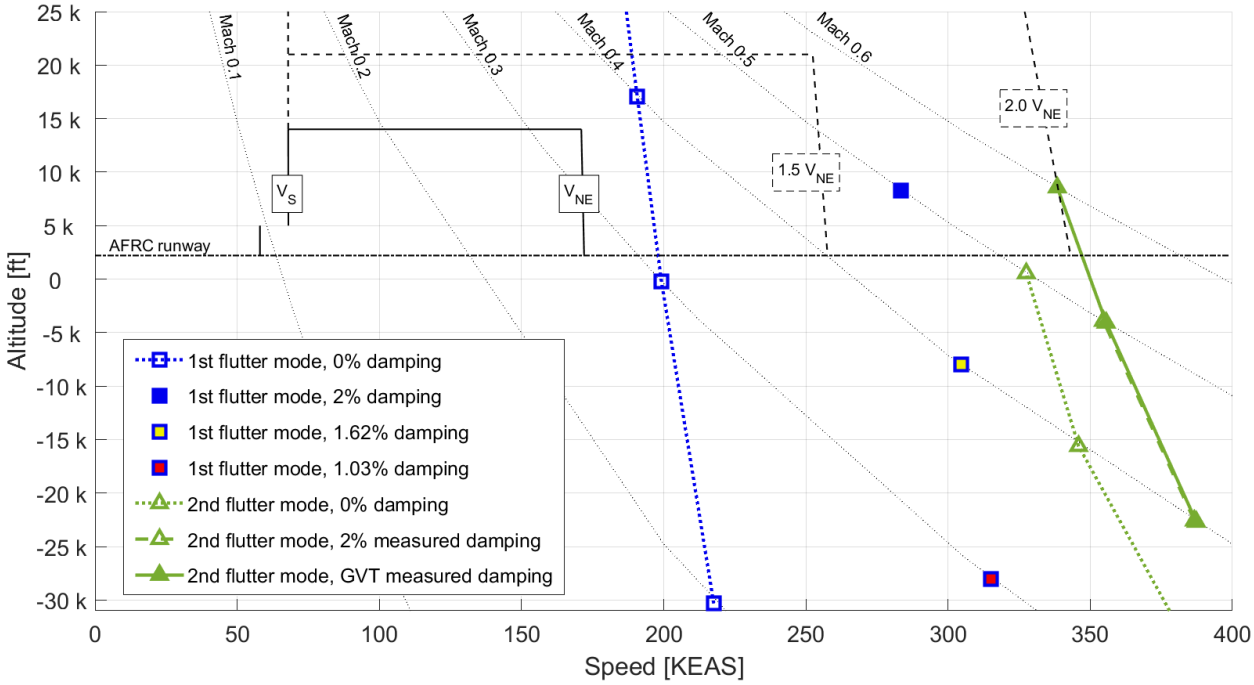

Fig. 13 The ZAERO-predicted flutter boundaries and flight envelope of the Mod II aircraft.

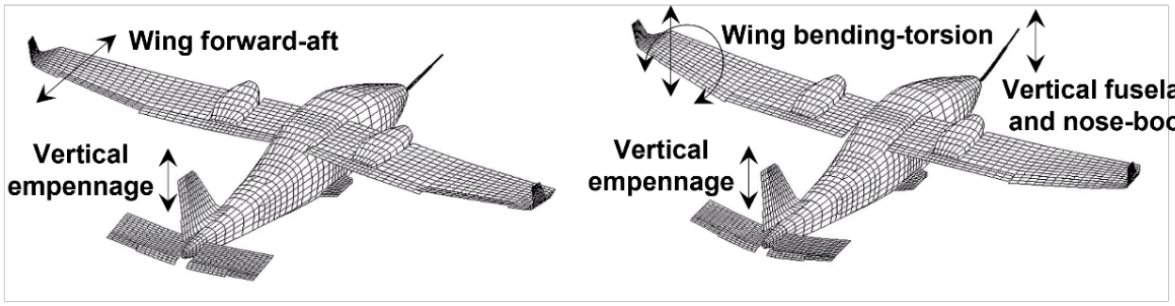

a) First flutter b) Second flutter

Fig. 14 The ZAERO-predicted flutter (aero-structure coupled) mode shapes of the Mod II aircraft.

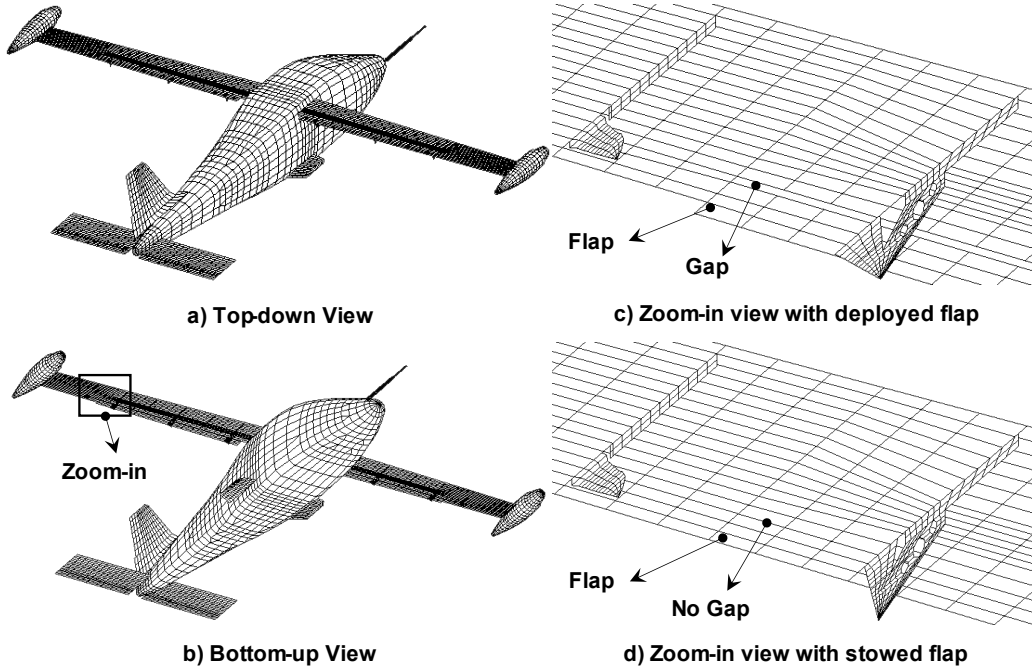

a) Top-down View c) Zoom-in view with deployed flap

b) Bottom-up View d) Zoom-in view with stowed flap

Fig. 15 The ZAERO unsteady aerodynamic model of the Mod III aircraft.

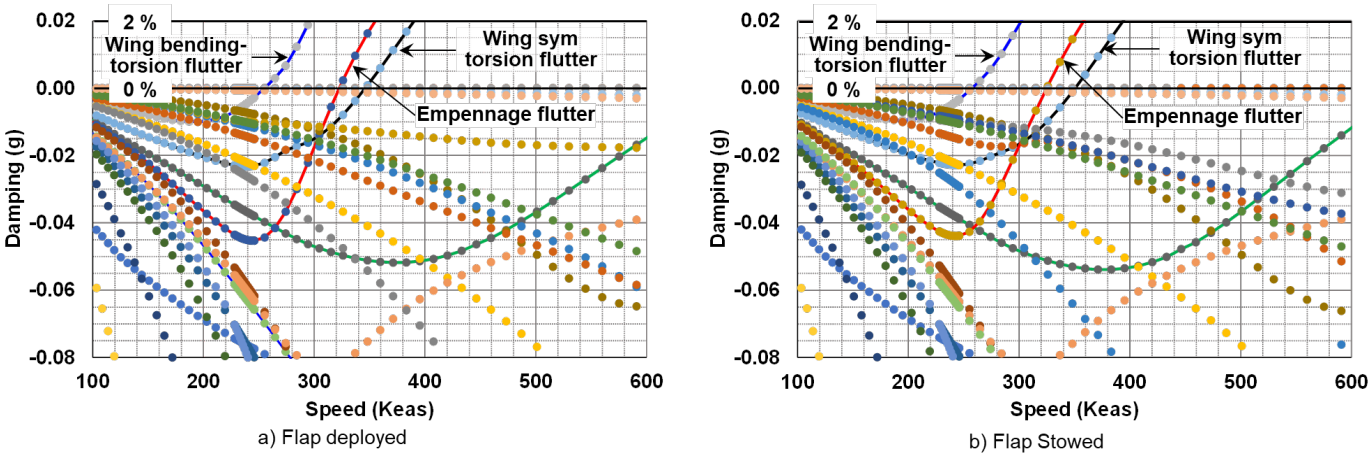

a) Flap deployed b) Flap Stowed

Fig. 16 The V-g curves of the Mod III aircraft at Mach 0.4.

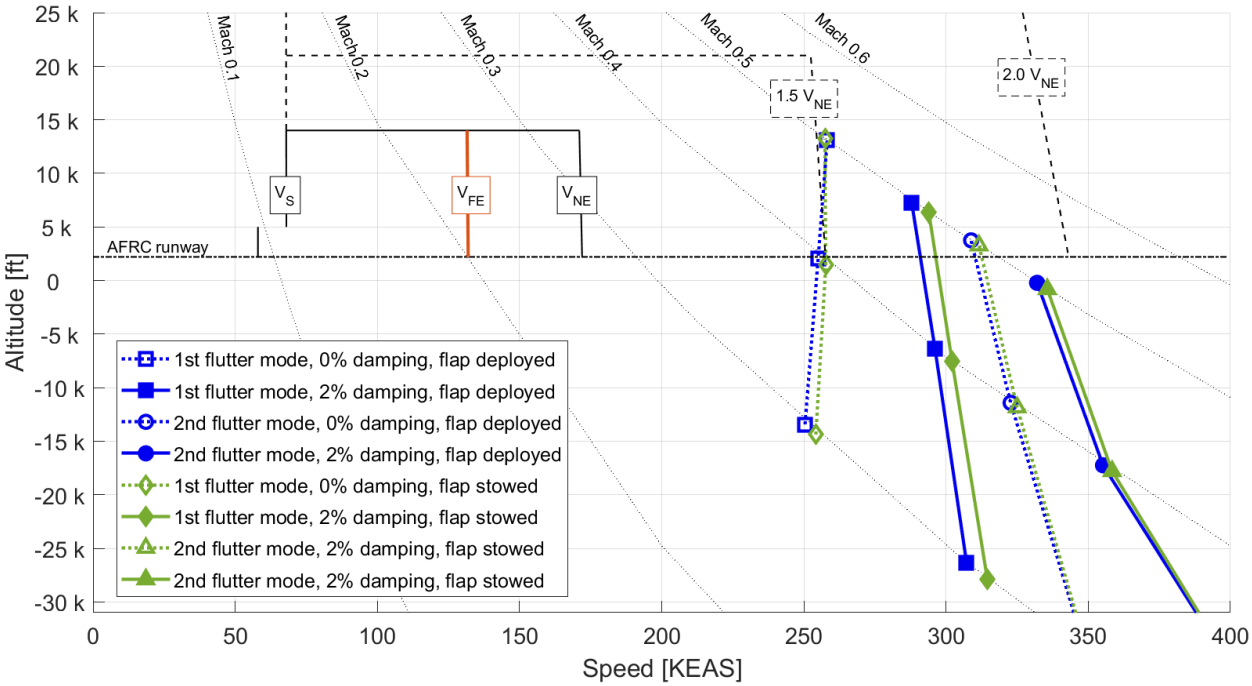

Fig. 17 The ZAERO-predicted flutter boundaries and flight envelope of the Mod III aircraft.

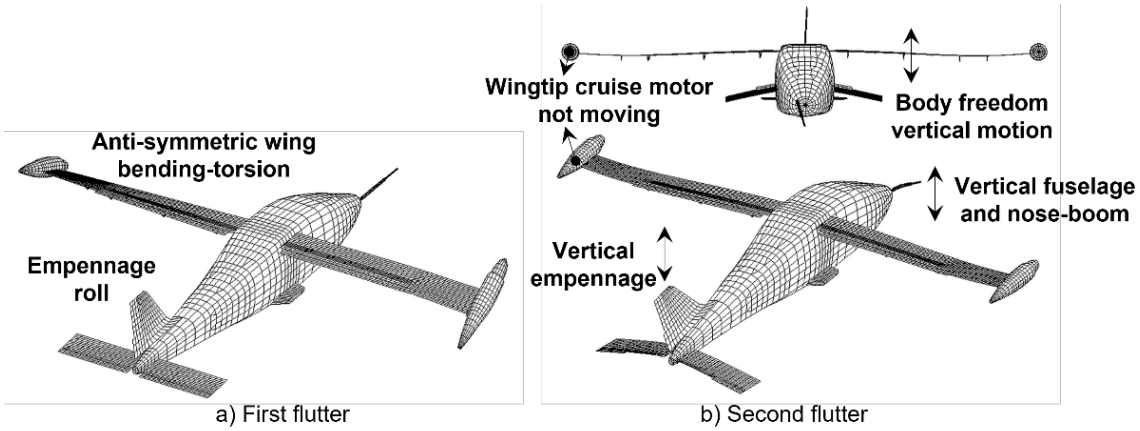

Fig. 18 The ZAERO-predicted flutter (aero-structure coupled) mode shapes of the Mod III aircraft.

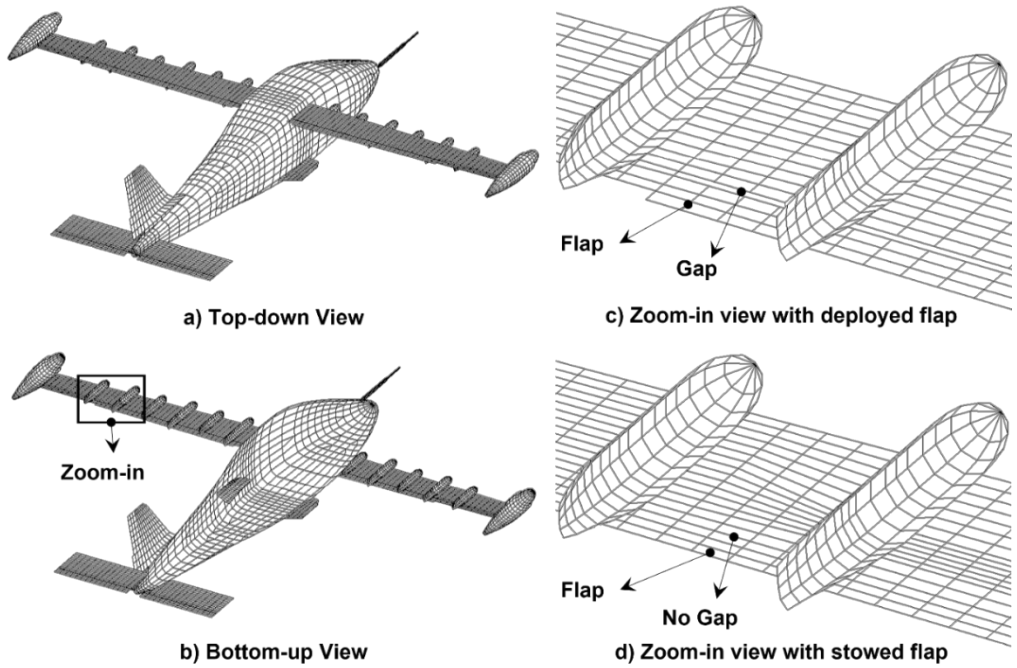

Fig. 19 The ZAERO unsteady aerodynamic model of the Mod IV aircraft.

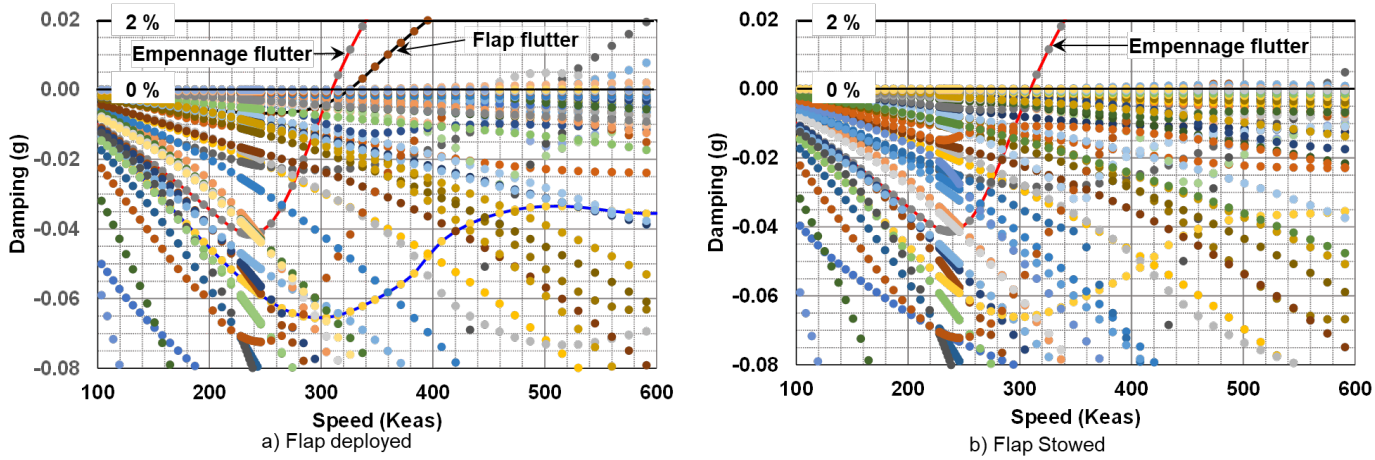

Fig. 20 The ZAERO-predicted V-g curves of the Mod IV aircraft at Mach 0.4.

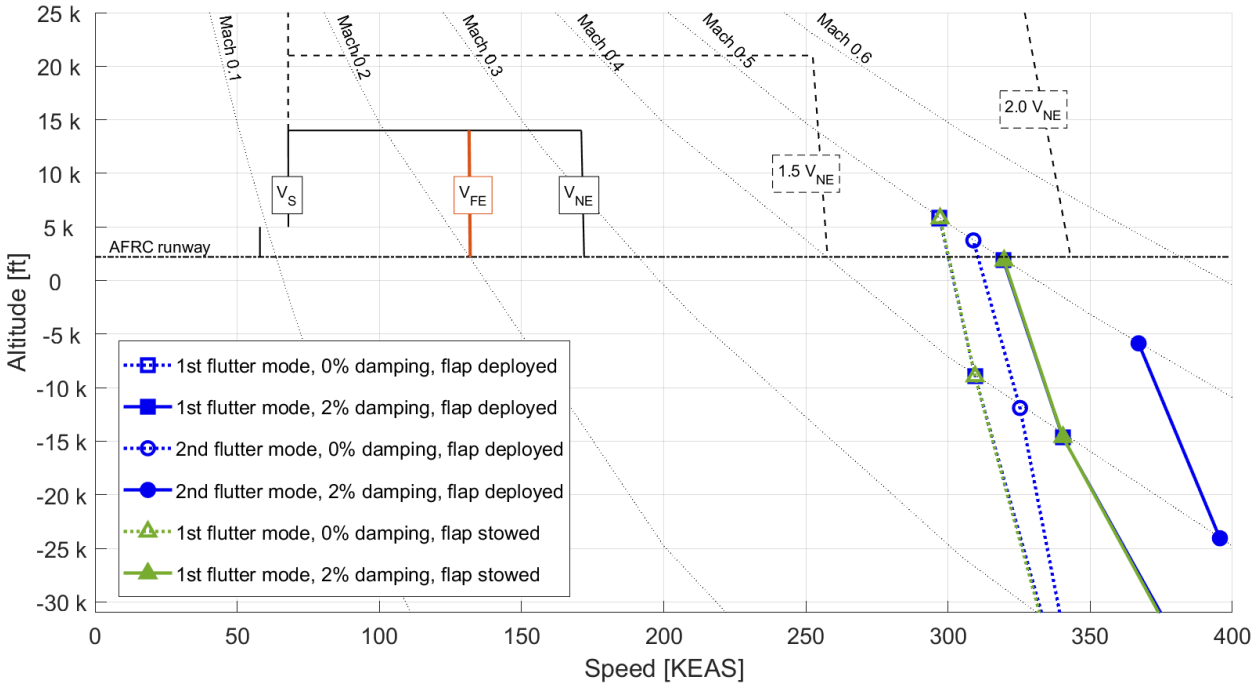

Fig. 21 The ZAERO-predicted flutter boundaries and flight envelope of the Mod IV aircraft.

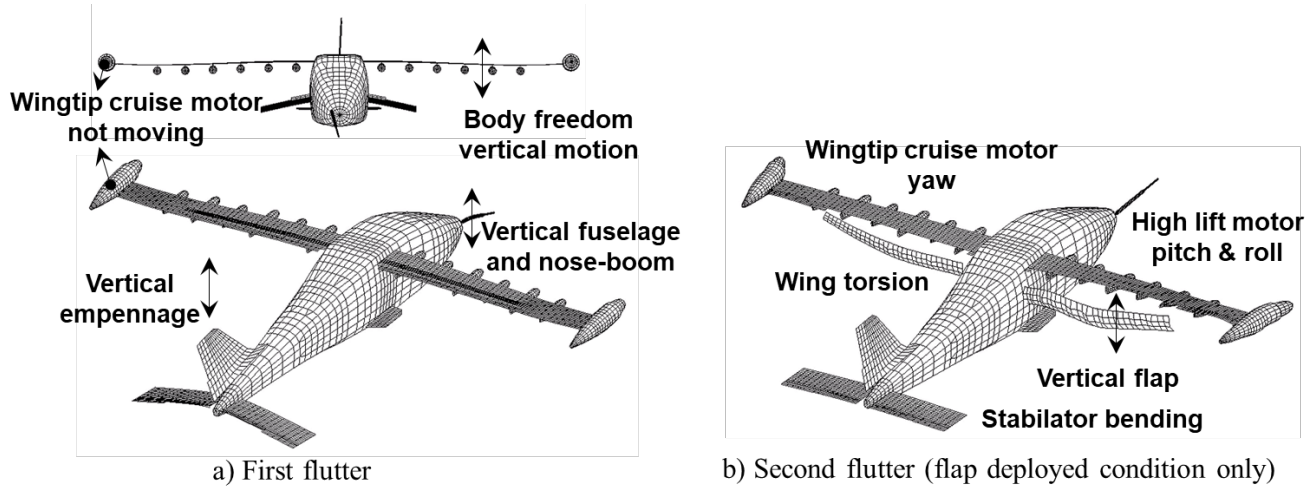

a) First flutter

b) Second flutter (flap deployed condition only)

Fig. 22 The ZAERO-predicted flutter (aero-structure coupled) mode shapes of the Mod IV aircraft.

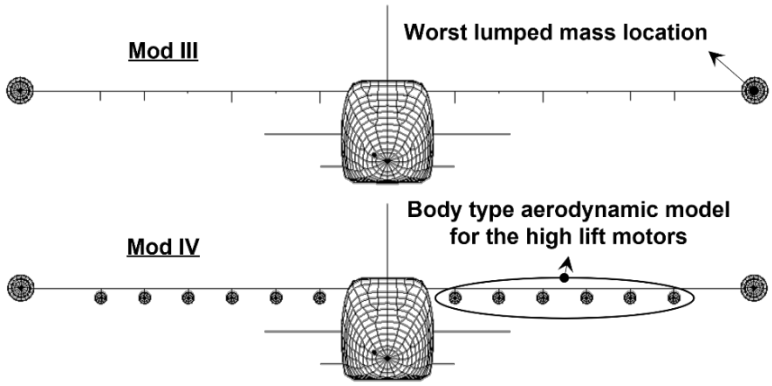

Fig. 23 Illustration of the Mod IV distributed high-lift motors which change the wing torsional stiffness of the Mod IV wing, and passively suppress the wing bending-torsion flutter mode predicted for the Mod III configuration.

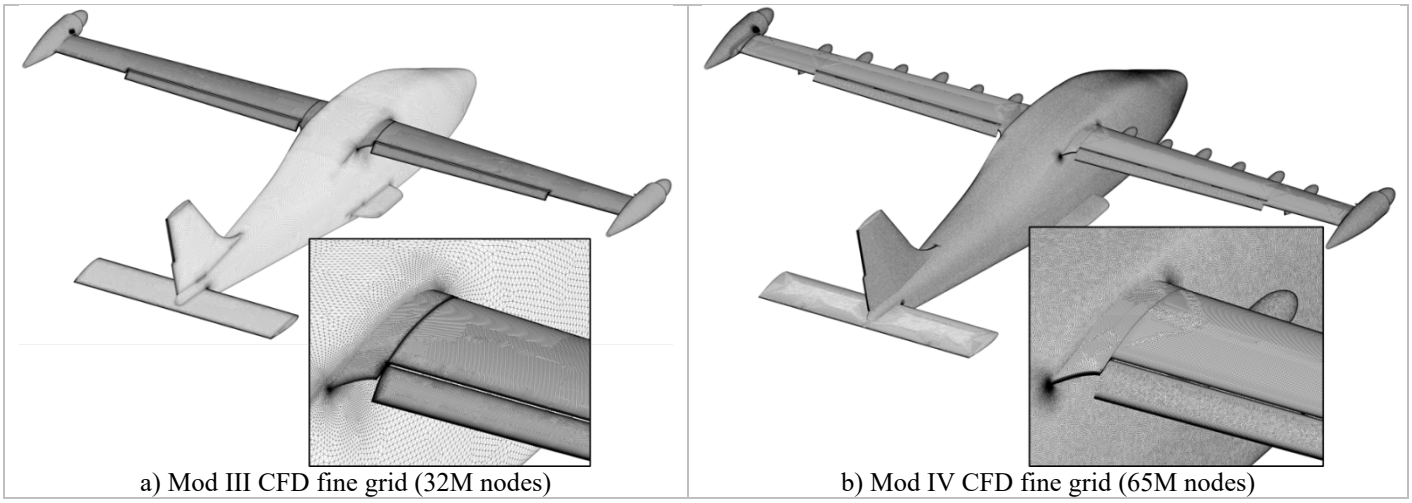

a) Mod III CFD fine grid (32M nodes) b) Mod IV CFD fine grid (65M nodes)

Fig. 24 Computational fluid dynamics grids used for Mod III and Mod IV FUN3D aeroelastic simulations.

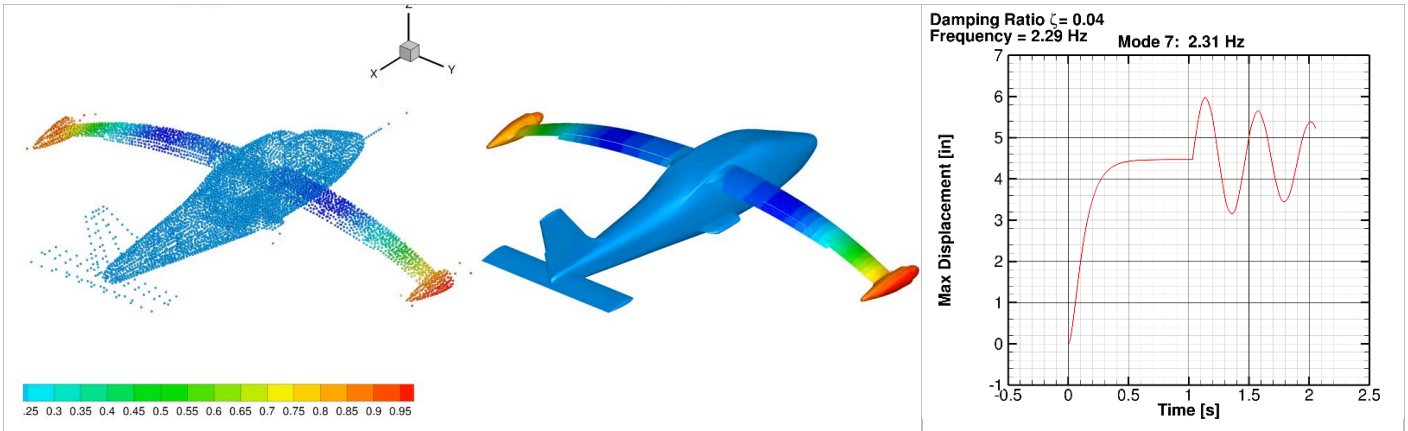

a) FEM nodes used for shape projection b) deformed CFD grid c) mode displacement time history

Fig. 25 Example of mode shape projection (left side) and mode perturbation stability (right side) from FUN3D aeroelastic simulations shown for Mod III first wing bending mode.

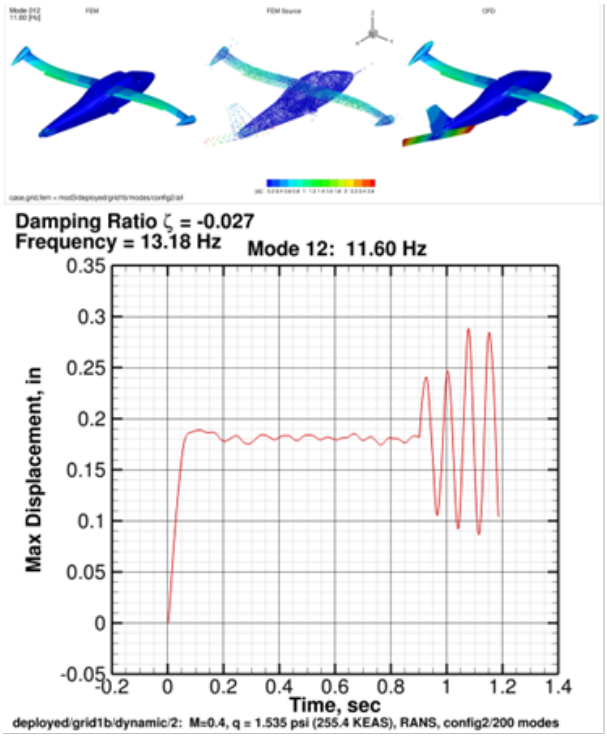

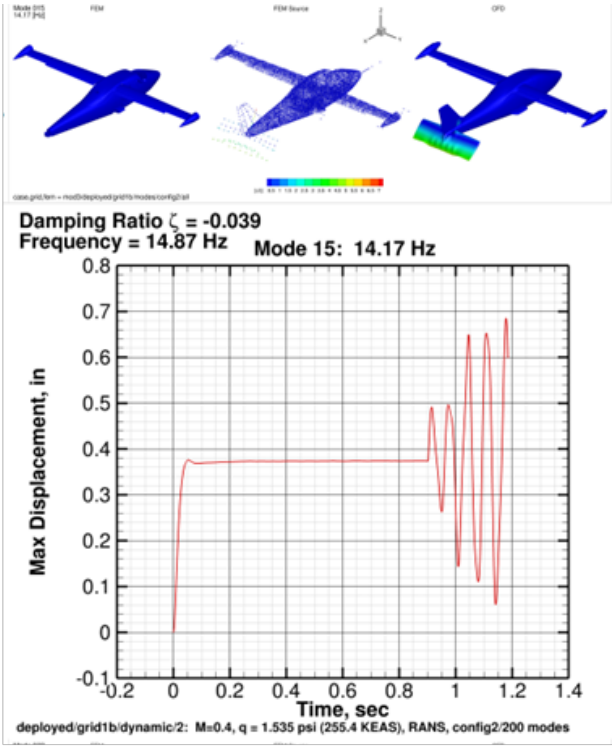

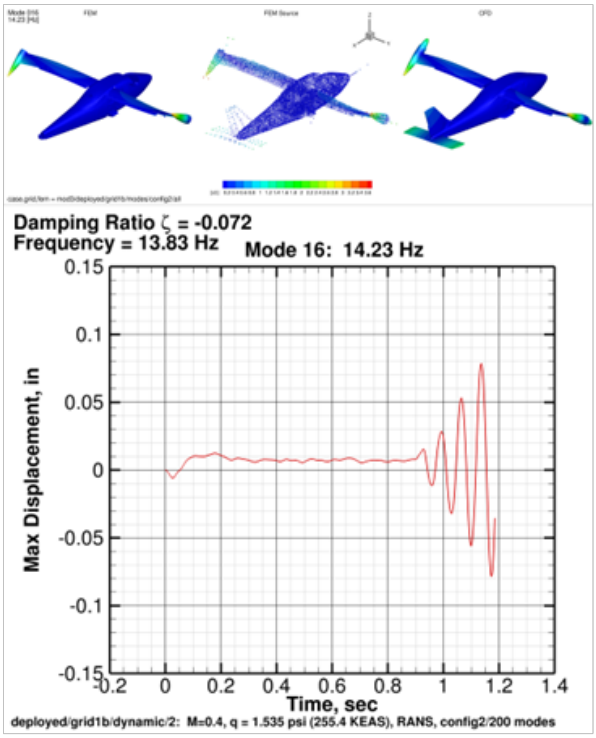

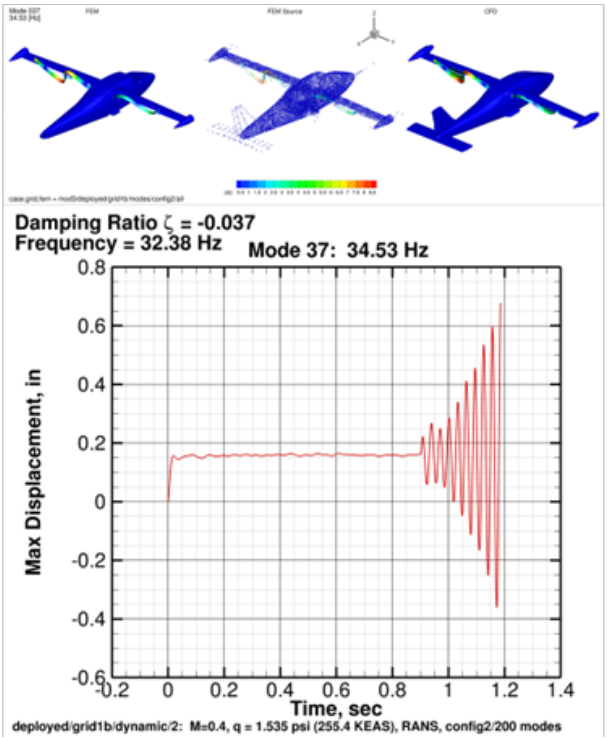

Fig. 26 Predicted modal responses from Mod III FUN3D aeroelastic simulation at Mach 0.4.